

A candidate redshift $z \approx 10$ galaxy and rapid changes in that population at an age of 500 Myr

R. J. Bouwens^{1,2}, G. D. Illingworth¹, I. Labbe³, P. A. Oesch⁴, M. Trenti⁵, C. M. Carollo⁴, P. G. van Dokkum⁶, M. Franx², M. Stiavelli⁷, V. González¹, D. Magee¹, L. Bradley⁷

¹*Department of Astronomy, University of California Santa Cruz, California 94064, USA*

²*Leiden Observatory, Leiden University, Leiden NL-2333, Netherlands*

³*Carnegie Observatories, Pasadena, California 91101, USA*

⁴*Institute for Astronomy, ETH Zurich, Zurich CH-8093, Switzerland*

⁵*University of Colorado, Center for Astrophysics and Space Astronomy, Boulder, Colorado 80303, USA*

⁶*Department of Astronomy, Yale University, New Haven, Connecticut 06520, USA*

⁷*Space Telescope Science Institute, Baltimore, Maryland 21218, USA*

Searches for very-high-redshift galaxies over the past decade have yielded a large sample of more than 6,000 galaxies existing just 900-2,000 million years (Myr) after the Big Bang (redshifts $6 > z > 3$; ref. 1). The Hubble Ultra Deep Field (HUDF09) data^{2,3} have yielded the first reliable detections of $z \approx 8$ galaxies³⁻⁹ that, together with reports of a γ -ray burst at $z \approx 8.2$ (refs 10, 11), constitute the earliest objects reliably reported to date. Observations of $z \approx 7-8$ galaxies suggest substantial star formation at $z > 9-10$ (refs 12, 13). Here we use the full two-year HUDF09 data to conduct an ultra-deep search for $z \approx 10$ galaxies in the heart of the reionization epoch, only 500 Myr after the Big Bang. Not only do we find one possible $z \approx 10$ galaxy candidate, but we show that, regardless of source detections, the star formation rate density is much smaller ($\sim 10\%$) at this time than it is just ~ 200 Myr later at $z \approx 8$. This demonstrates how rapid galaxy build-up was at $z \approx 10$, as galaxies increased in both luminosity density and volume density from $z \approx 8$ to $z \approx 10$. The 100-200 Myr before $z \approx 10$ is clearly a crucial phase in the assembly of the earliest galaxies.

The detection of galaxies at very high redshift from deep imaging data depends on the absorption (by intervening neutral hydrogen) of much of the flux in the spectrum at wavelengths below the wavelength of Lyman α (121.6 nm). These spectral breaks shift to longer wavelengths for more distant, redshifted galaxies seen at earlier times. A distinguishing characteristic of $z \approx 10$ galaxies would be, first, a detection in the H_{160} band, and, second, the absence of flux in the J_{125} band, and in all other shorter-wavelength Hubble Space Telescope (HST) Wide Field Camera 3 (WFC3/IR) and Advanced Camera for Surveys (ACS) filters blueward of the J_{125} band (hence they are called

J_{125} -dropouts). The new, powerful HST WFC3/IR camera is ~ 40 times more efficient at finding $z \approx 7$ galaxies^{2,4–9} than the previous near-infrared NICMOS camera owing to its wider field of view and greater sensitivity in its Y_{105} , J_{125} and H_{160} filters. It provides us with the capability to explore to $z \approx 10$.

A thorough search of the deep WFC3/IR HUDF09 data set strong limits at $z \approx 10$, and also resulted in the detection of a candidate $z \approx 10$ J_{125} -dropout galaxy UDFj-39546284 at 5.4σ in our $0.26''$ -diameter selection aperture (Fig. 1). The signal-to-noise ratio grows to 5.8σ in a larger $0.35''$ -diameter aperture. The candidate is 28.92 ± 0.18 mag in the WFC3/IR H_{160} band ($(1.01 \pm 0.18) \times 10^{31}$ erg s⁻¹ cm⁻² Hz⁻¹), has a likely redshift of $z \approx 10.3$ (Fig. 2), and appears to be slightly extended. Given the importance of the limits that we set, and of the candidate $z \approx 10$ galaxy, we perform extensive tests and simulations. These are described in Supplementary Information sections 4 and 7, while the candidate properties are given in Supplementary Table 1.

The existence of galaxies at $z > 8.2$ (the γ -ray burst redshift^{10,11}) is strengthened by three additional sources that have been detected in recent searches^{3–9}, one of which has a tentative spectroscopic confirmation at $z \approx 8.6$ (ref. 14). The updated redshift distributions from our simulations show that these three sources³ are most likely to be at $z \approx 8.7$, 8.5 and 8.6 (Fig. 2). The expectation of finding galaxies at $z \approx 10$, just ~ 120 Myr earlier, is enhanced by these strong detections at $z \approx 8.5$, especially since the $z \approx 7$ -8 Spitzer and HST data suggest that substantial star formation is likely at $z > 9$ -10 (refs 12, 13).

The photometric-selection dropout approach has been verified through numerous spectroscopic confirmations at redshifts from $z \approx 2$ to $z \approx 6$ (refs 15-19), and possibly also now at $z \approx 8.6$ (ref. 14). For our candidate $z \approx 10$ galaxy, however, its single band (H_{160} band) detection increases the risk of contamination compared to the $z \approx 7$ and $z \approx 8$ samples, where two (or more) bands are used to measure the source magnitudes and colours. Fortunately, we can test the robustness of the single-band detection process by selecting $z \approx 8$ galaxy candidates using the J_{125} -band data alone. Analogous to the $z \approx 10$ J_{125} -dropouts, $z \approx 8$ galaxies are Y_{105} -band dropouts. We compare this single-band selection against the more robust $z \approx 8$ detections using two bands³ (J_{125} and H_{160}). We are very encouraged that we select the same eight $z \approx 8$ Y_{105} -dropouts with the J_{125} -band data alone, as we do with the normal selection using the J_{125} and H_{160} -band data. The primary reason for the robustness is the non-detection in all shorter wavelength filters. The χ_{opt}^2 test that we have developed⁹ largely eliminates contaminating objects.

Our $z \approx 10$ candidate was also checked for any Spitzer IRAC flux in the $3.6\mu\text{m}$ band (see Fig. 1). It is quite isolated and is not detected to ~ 27 AB mag (2σ), further enhancing the case that this $z \approx 10$ candidate corresponds to a very-high-redshift galaxy rather than a highly reddened, lower-redshift contaminant. Contamination from spurious sources is also an important concern for such faint sources. We verified that the source is present in a wide variety of subsets of the H_{160} -band data (Fig. 1, Supplementary Fig. 2), suggesting that the candidate is not spurious. Although these tests make the case for this source being a $z \approx 10$ galaxy, deeper observations –

involving both imaging (with, for example, WFC3/IR) and spectroscopy (with the James Webb Space Telescope) – will be required to confirm it.

Using the results of these tests and Monte Carlo simulations, we estimate there is an $\sim 20\%$ probability that our candidate is a contaminant or is spurious. Of that 20%, 10% was estimated to be from photometric scatter. Contamination from spurious sources is uncertain, and our estimates range from 1% to 10% probability; to be conservative we adopt 10%. Contamination from lower-redshift red sources is also possible, but the above single-filter $z \approx 8$ Y_{105} -dropout test suggests that the probable contamination is small, consistent with the totals we estimate from our other tests ($\sim 20\%$).

Fortunately, the depth of the data and the thoroughness of our analysis for contamination allow us to set very strong constraints on the volume density of $z \approx 10$ galaxies, regardless of the uncertainties associated with our candidate $z \approx 10$ galaxy. Thus we evaluate our constraints based on the limit set if no galaxies were found, and based on the candidate $z \approx 10$ galaxy, whose volume density is corrected by 20% to account for the estimated contamination rate.

Large-scale structure uncertainties are important for small-area searches. We estimate the field-to-field variance on the present $z \approx 10$ J_{125} -dropout searches in the HUDF09 field to be 39% (see Supplementary Information)²⁰. Even at this level, the cosmic variance (large-scale structure) is not the dominant source of uncertainty for our single candidate galaxy.

These $z \approx 10$ results have far-reaching implications for estimating the role of galaxies in reionization (using the luminosity density), and for establishing the star formation rate density at very early times, as $z \approx 10$ is just 480 Myr after the Big Bang and just a few hundred million years since the first galaxies formed. The upper limits and our candidate allow us to do this through quantitative constraints we place on the $z \sim 10$ luminosity function.

The extent of the changes at $z \approx 10$ can be demonstrated by first contrasting what we see at $z \approx 10$ with expectations based on a no-evolution scenario: that is, the galaxy populations stay unchanged with time. We compute the no-evolution estimate by using our galaxy cloning software²¹ to artificially redshift the observed $z \approx 6$ and $z \approx 7$ galaxy population to $z \approx 10$, add them at random positions within our HUDF data, and then repeat the object selection process just as for the observed $z \approx 10$ galaxy sample. We estimated that we would find 12 ± 4 $z \approx 10$ galaxies using our $z \approx 7$ detections as the baseline, and 23 ± 5 $z \approx 10$ galaxies using our $z \approx 6$ detections as a baseline. These no-evolution estimates are substantially higher than our (contamination-corrected) estimate of ~ 0.8 $z \approx 10$ galaxies. For simple Poissonian statistics, our observed number of ~ 0.8 galaxies is inconsistent with no-evolution at 4σ and 5σ confidence, respectively (and sets even stronger limits on any upturn in the star formation rate⁶). Although striking, this is not wholly unexpected. Extrapolating the trends seen by us at lower redshifts²² would lead us to expect 3 ± 2 $z \approx 10$ sources. Thus our results reaffirm that the significant evolution seen in galaxies at lower redshift continues to $z \approx 10$ (in contrast with other studies⁶).

The present search results can also be expressed as constraints on the luminosity function at $z \approx 10$. The luminosity function describes the number density of galaxies versus luminosity, and is important for estimating the ultraviolet flux from galaxies and their expected role in reionizing the Universe. The high-redshift-galaxy ultraviolet luminosity function maintains a nearly constant form and evolves in a largely self-similar manner, with the characteristic luminosity (L^*) increasing smoothly over about 1,300 Myr from $z \approx 7$ to $z \approx 3$, that is, from ~ 750 Myr to $\sim 2,000$ Myr. Assuming the same form for the ultraviolet luminosity function at $z \sim 10$, we find that L^* at $z \approx 10$ is fainter, indicating that the evolution in the bright end of the ultraviolet luminosity function seen from $z \approx 7$ to $z \approx 4$ (refs 1, 9, 22) continues to $z \approx 10$ (Fig. 3). Definitive measurements of L^* at $z \approx 10$ will, of course, require deep, wide-area data to define the luminous end of the $z \approx 10$ luminosity function.

The existence of a steep slope α to the faint end of the ultraviolet luminosity function found at $z \approx 6-7$ (refs 1, 2, 9) highlights the importance of low luminosity galaxies in providing the flux needed to reionize the Universe. It is of great interest to estimate the ultraviolet luminosity density at $z \approx 7-10$ where reionization most probably occurred, given its apparent completion at $z \approx 6$ (ref. 23) and its onset at $z \approx 11$ as deduced from Wilkinson Microwave Anisotropy Probe (WMAP)²⁴ observations. The recent results from the HUDF09 data set provide estimates for the ultraviolet luminosity density at $z \approx 7$ and at $z \approx 8$ (ref. 9). We can now also do so at $z \approx 10$. We compute the luminosity density implied by our sample by assuming a faint-end slope of -1.7 (the same slope as found for the $z \approx 2-7$ luminosity functions) and extending the integration down to a very plausible limit of -12 AB mag. We find that the ultraviolet flux that is available from galaxies at $z \approx 10$ is only $\sim 12^{+26}_{-10}\%$ of what is needed for galaxies to be the reionizing source, with typical assumptions of an escape fraction of ~ 0.4 , a clumping factor of ~ 3 and a Salpeter initial mass function (see, for example, ref. 9). This result is tantalizing, suggesting that galaxies are contributing to reionization, but the enigma remains: where are most of the needed ultraviolet photons coming from? Observations to significantly fainter levels will be central to characterizing the role of galaxies in reionization.

The star formation rate (SFR) density is derived from the luminosity density (see Fig. 4). The SFR density increases systematically and monotonically at early times from $z \approx 10$ (500 Myr) to $z \approx 4$ (1,600 Myr), peaking at $z \approx 2-3$ (at $\sim 2,500$ Myr), before decreasing at $z < 2$ (Fig. 4). This suggests that the luminosity function and star formation rate density evolution found at lower redshifts^{1,25} continues to $z \approx 10$ when the universe was just 480 Myr old. The limits established here even suggest that the trends in star formation rate density established at lower redshifts could be steepening.

This is clearly an era when galaxies were evolving very rapidly. The star formation rate density increased by a factor of ~ 10 in less than 200 Myr, from $z \approx 10$ to $z \approx 8$. This dramatic change in such a short period of time suggests that the first phases of galaxy formation and their build-up could be unveiled by observations that penetrate just 200 Myr earlier, to redshifts $z \approx 15$. However, only when the James Webb Space Telescope is launched will these first phases of galaxy build-up

between $z \approx 15$ and $z \approx 10$ be revealed.

Received 21 December 2009

1. Bouwens, R.J., Illingworth, G.D., Franx, M., & Ford, H. UV Luminosity Functions at $z \sim 4$, 5, and 6 from the Hubble Ultra Deep Field and Other Deep Hubble Space Telescope ACS Fields: Evolution and Star Formation History. *Astrophys. J.* **670**, 928-958 (2007).
2. Oesch, P.A., *et al.* $z \sim 7$ Galaxies in the HUDF: First Epoch WFC3/IR Results. *Astrophys. J. Lett.* **709**, L16-L20 (2010).
3. Bouwens, R.J., *et al.* Discovery of $z \sim 8$ Galaxies in the HUDF from ultra-deep WFC3/IR Observations. *Astrophys. J. Lett.* **709**, L133-L137 (2010).
4. McLure, R., *et al.* Galaxies at $z \sim 6 - 9$ from the WFC3/IR imaging of the HUDF. *Month. Not. R. Astron. Soc.* **403**, 960-983 (2010).
5. Bunker, A., *et al.* The Contribution of High Redshift Galaxies to Cosmic Reionization: New Results from Deep WFC3 Imaging of the Hubble Ultra Deep Field. *Month. Not. R. Astron. Soc.* **409**, 855-866 (2010).
6. Yan, H., *et al.* Galaxy Formation In The Reionization Epoch As Hinted By Wide Field Camera 3 Observations Of The Hubble Ultra Deep Field. *Res. Astron. Astrophys.* **10**, 867-904 (2010).
7. Finkelstein, S. *et al.* On the Stellar Populations and Evolution of Star-Forming Galaxies at $6.3 < z < 8.6$. *Astrophys. J.* **719**, 1250-1273 (2010).
8. Robertson, N., Ellis, R. S., Dunlop, R. S., McLure, R. J. & Stark, D. P. Early star-forming galaxies and the reionization of the Universe. *Nature* **468**, 49-55 (2010).
9. Bouwens, R. J. *et al.* UV luminosity functions from 113 $z \sim 7$ and $z \sim 8$ Lyman-break galaxies in the ultra-deep HUDF09 and wide-area ERS WFC3/IR observations. 2010. *Astrophys. J.* (submitted); preprint at <http://arxiv.org/abs/1006.4360> (2010).
10. Tanvir, N., *et al.* A γ -ray burst at a redshift of $z \sim 8$. *Nature* **461**, 1254-1257
11. Salvaterra, R., *et al.* GRB090423 at a redshift of $z \sim 8.1$. *Nature* **461**, 1258-1260
12. Labbe, I., *et al.* Ultradeep IRAC Observations of sub- L^* $z \sim 7$ and $z \sim 8$ Galaxies in the HUDF: the Contribution of Low-Luminosity Galaxies to the Stellar Mass Density and Reionization. *Astrophys. J. Lett.* **708**, L26-L31 (2010).
13. Gonzalez, V. *et al.* Stellar Mass Density and Specific Star Formation Rates of the Universe at $z \sim 7$, *Astrophys. J.* **713**, 115-130 (2010).
14. Lehnert, M. *et al.* Spectroscopic confirmation of a galaxy at $z \sim 8.6$. *Nature* **467**, 940-942 (2010).

15. Steidel, C.C., Giavalisco, M., Pettini, M., Dickinson, M., & Adelberger, K.L. Spectroscopic Confirmation of a Population of Normal Star-forming Galaxies at Redshifts $Z > 3$. *Astrophys. J. Lett.* **462**, 17-20 (1996).
16. Vanzella, E., *et al.* Spectroscopic Observations of Lyman Break Galaxies at Redshifts ~ 4 , 5, and 6 in the GOODS-South Field. *Astrophys. J.* **695**, 1163-1182 (2009).
17. Popesso, P. *et al.* The great observatories origins deep survey. VLT/VIMOS spectroscopy in the GOODS-south field. *Astron. Astrophys.* **494**, 443-460 (2009).
18. Steidel, C.C. *et al.* Lyman Break Galaxies at Redshift $z \sim 3$: Survey Description and Full Data Set. *Astrophys. J.* **592**, 728-754 (2003).
19. Reddy, N. *et al.* A Spectroscopic Survey of Redshift $1.4 < z < 3.0$ Galaxies in the GOODS-North Field: Survey Description, Catalogs, and Properties. *Astrophys. J.* **653**, 1004-1026 (2006).
20. Trenti, M. & Stiavelli, M. Cosmic Variance and its Effect on the Luminosity Function Determinations in Deep High- z Surveys. *Astrophys. J.* **676**, 767-780 (2008).
21. Bouwens, R.J., Broadhurst, T.J., Silk, J. Cloning Hubble Deep Fields. I. A Model-independent Measurement of Galaxy Evolution. *Astrophys. J.* **506**, 557-578 (1998).
22. Bouwens, R.J., Illingworth, G.D., Franx, M., & Ford, H. $z \sim 7$ -10 Galaxies in the HUDF and GOODS Fields: UV Luminosity Functions. *Astrophys. J.* **686**, 230-250 (2008).
23. Fan, X., *et al.* Evolution of the Ionizing Background and the Epoch of Reionization from the Spectra of $z \sim 6$ Quasars. *Astronom. J.* **123**, 1247-1257 (2002).
24. Komatsu, E., *et al.* Seven-Year Wilkinson Microwave Anisotropy Probe Observations: Cosmological Interpretation. *Astrophys. J.* (in press); preprint at <<http://arXiv.org/abs/1001.4538>> (2010).
25. Bouwens, R., *et al.* UV-Continuum Slope and Dust Obscuration from $z \sim 6$ to $z \sim 2$: The Star Formation Rate Density at High Redshift. *Astrophys. J.* **705**, 936-961 (2009).
26. Beckwith, S.W., *et al.* The Hubble Ultra Deep Field. *Astrophys. J.* **132**, 1729-1755 (2006).
27. Reddy, N., & Steidel, C.C. A Steep Faint-End Slope of the UV Luminosity Function at $z \sim 2$ -3: Implications for the Global Stellar Mass Density and Star Formation in Low-Mass Halos. *Astrophys. J.* **692**, 778-803 (2009).
28. Yoshida, M., *et al.* Luminosity Functions of Lyman Break Galaxies at $z \sim 4$ and $z \sim 5$ in the Subaru Deep Field. *Astrophys. J.* **653**, 988-1003 (2006).
29. McLure, R., Cirasuolo, M., Dunlop, J.S., Foucaud, S., Almaini, O. The luminosity function, halo masses, and stellar masses of luminous Lyman-break galaxies at $5 < z < 6$. *Month. Not. R. Astron. Soc.* **395**, 2196-2209 (2009).

30. Schiminovich, D., *et al.* The GALEX-VVDS Measurement of the Evolution of the Far-Ultraviolet Luminosity Density and the Cosmic Star Formation Rate. *Astrophys. J. Lett* **619**, 47-50 (2005).

Supplementary Information is linked to the online version of the paper at www.nature.com/nature.

Acknowledgements We are grateful to all those at NASA, STScI and throughout the community who have worked to make the Hubble Space Telescope the observatory that it is today, and we acknowledge the importance of the servicing missions and those who organised them. We acknowledge our program coordinator W. Januszewski for his care in helping to set up our program and observing configuration. We acknowledge support from NASA and the Swiss National Science Foundation.

Author Contributions R.J.B. carried out the most of the data analysis and calculations for this paper, and wrote most of the Supplementary Information; G.D.I. wrote most of the text in the Letter and iterated on the initial science results and content with R.J.B.; I.L., P.A.O., M.T., C.M.C., P.G.v.D., M.F., M.S. and L.B. provided significant feedback on the science content and on the drafts; I.L. and V.G. were involved with processing the Spitzer IRAC data; P.A.O. contributed to the data analysis; M.T. made the cosmic variance estimates; and D.M. was involved in data processing and pipeline generation for the WFC3/IR data.

Author Information Reprints and permissions information is available at www.nature.com/reprints. The authors declare no competing financial interests. Readers are welcome to comment on the online version of this article at www.nature.com/nature. Correspondence and requests for materials should be addressed to R.J.B. (bouwens@ucolick.org).

UDFj-39546284 $H=28.9$ $J-H>2.0$

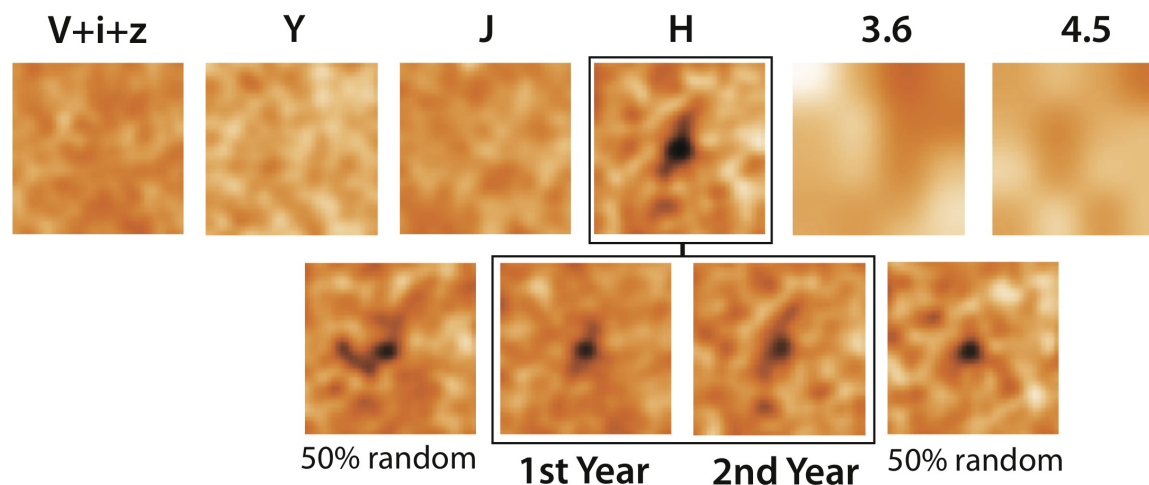


Figure 1. Optical and near-infrared images of the candidate $z \approx 10$ galaxy, UDFj-39546284, from the HUDF. Top row: the leftmost panel shows the HUDF ACS ($V_{606}i_{775}z_{850}$) data²⁶; the next

three panels show the similarly deep HUDF09 (HST GO 11563), near-infrared WFC3/IR (Y_{105} , J_{125} , H_{160}) data (reaching to 5σ depths of ~ 29.8 AB mag)^{2,3,9}; and the last two panels show the longer wavelength Spitzer IRAC 3.6 and 4.5 μm observations. Bottom row: the two middle panels show images of our $z \approx 10$ candidate in the first and second year of H_{160} -band observations (each representing $\sim 50\%$ of the total); the two outer panels show two random 50% subsets of the data (see also Supplementary Fig. 2). Each cutout is $2.4'' \times 2.4''$ on a side, and is orientated with north at the top. For our selection criteria, we require our $z \approx 10$ candidates to be detected at 5σ in the H_{160} band, to have $J_{125} - H_{160}$ colours redder than 1.2 AB mag, and to be undetected ($< 2\sigma$) in all imaging observations blueward of the J_{125} band. Also, candidates must not be detected at $> 1.5\sigma$ in more than one band blueward of the J_{125} band, and have $\chi^2 < 2.5$ in the extremely-deep image obtained by combining the B_{435} , V_{606} , i_{775} , z_{850} and Y_{105} imaging data. All of these requirements place very strong limits on the optical flux from our $z \approx 10$ candidates and provide strong discrimination against contamination by low-redshift sources (see ref. 9, Appendix C). The candidate is significant at $> 3\sigma$ in each year of observations and therefore not likely to be spurious. It is detected at 5.4σ in the H_{160} band, which is much more significant than the next possible candidates (seen at 4.0σ and 4.9σ). In addition, our $z \approx 10$ candidate is not detected in the IRAC data, as expected given the IRAC flux limits. The position and other properties of this candidate are given in Supplementary Table 1.

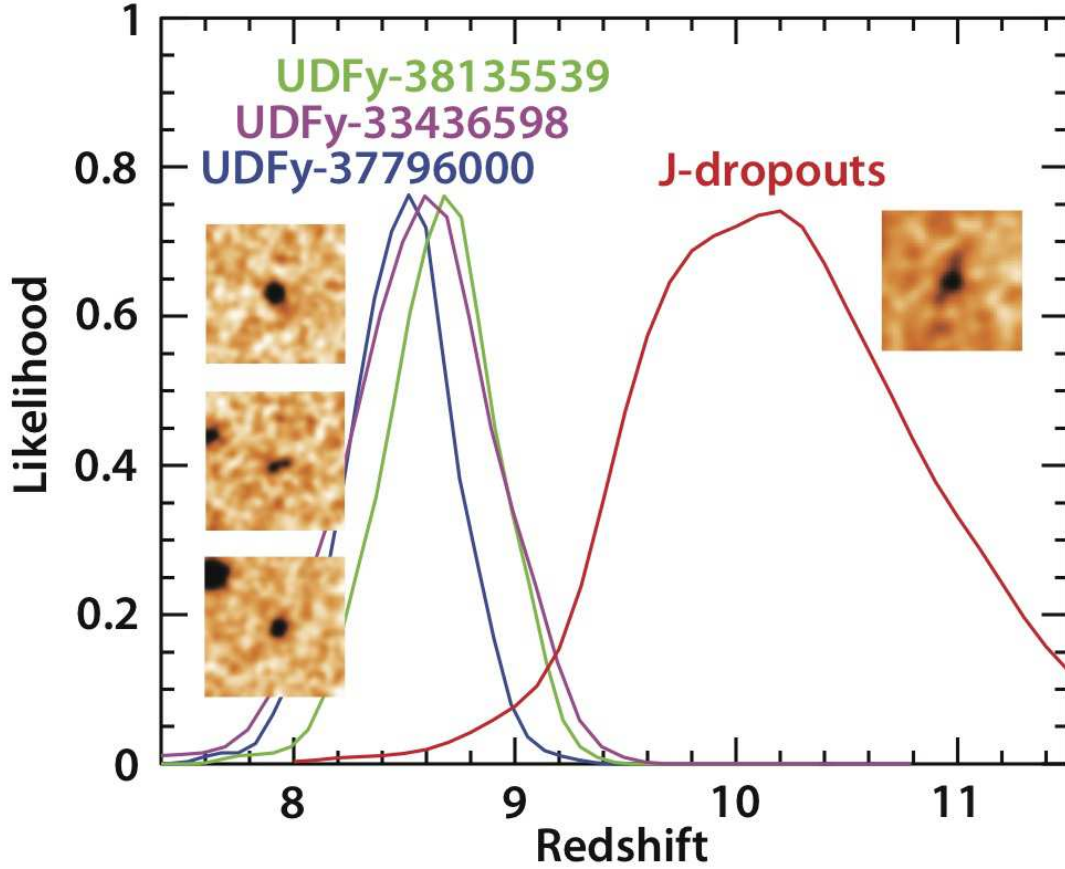


Figure 2. Predicted redshift distributions for our $z \approx 8.5$ and $z \approx 10$ galaxy candidates. The red line gives the redshift distribution for our $z \approx 10$ J_{125} -dropout candidate, while the blue, green and magenta lines give the redshift distributions for our $z \approx 8.5$ Y_{105} -dropout candidates. The H_{160} -band source images that correspond to the redshift distributions are shown for the $z \approx 8.7$, 8.6 and $z \approx 8.5$ sources (labels arranged in same order as images), and for our $z \approx 10.3$ candidate. Each source image is $2.4'' \times 2.4''$, with north at the top. The selection criteria for the $z \approx 8-9$ sources have been published elsewhere^{3,9} (see also Supplementary Information section 5). However, the detailed redshift distributions are shown here for the first time. The redshift distributions were derived by adding artificial sources to the HUDF09 WFC3/IR data, and reselecting them in the same way as the actual galaxy candidates (see Supplementary Information sections 4, 5 and 9). The mean redshifts of these distributions are 8.7, 8.6, 8.5 and 10.3. The $z \approx 8.7$ source has a tentative spectroscopic confirmation at $z \approx 8.6$ (ref. 14). For these simulations, the ultraviolet luminosity function was used. The luminosity function describes the number density of galaxies

versus luminosity and is usually parameterized as $\phi^* e^{-L/L^*} (L/L^*)^\alpha$, where ϕ^* is the normalization, L^* is the characteristic luminosity, and α is the faint end slope (see Fig. 3). The luminosity function was assumed to have an M_{UV}^* of -19.5 and -18.8 at $z \approx 8$ and $z \approx 10$, respectively (based on predictions from our $z \approx 4-7$ fitting relation^{9,22}), while α was taken to be -1.74 .

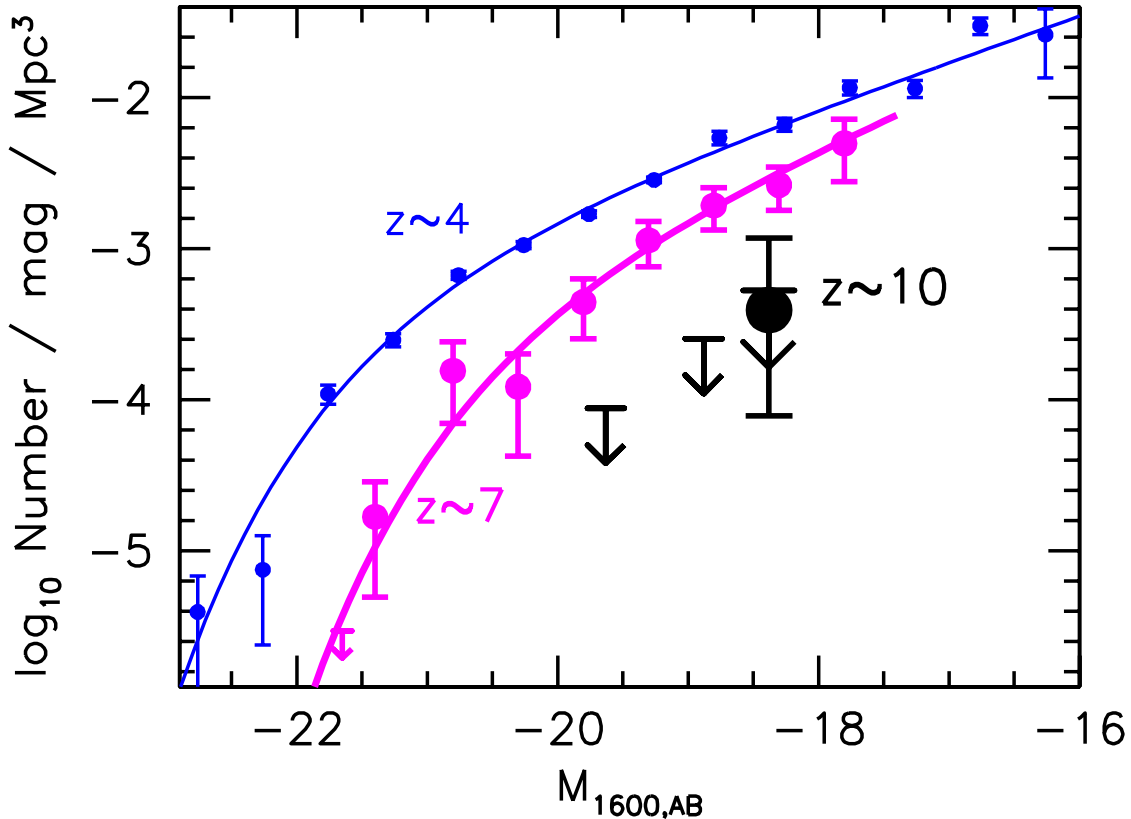


Figure 3. Ultraviolet luminosity functions at $z \approx 4$, $z \approx 7$ and constraints for $z \approx 10$. The present constraints on the stepwise ultraviolet luminosity function at $z \approx 10$ (black points and upper limits) are new and are derived from the J_{125} -dropout candidate galaxies over our ultra-deep HUDF WFC3/IR field. These luminosity functions are a function of the absolute magnitude (that is, luminosity) of galaxies ($M_{1600,AB}$) in the rest-frame far-ultraviolet. All error bars are 1σ . The stepwise luminosity function at $z \approx 10$ is also presented as a 1σ upper limit, given the uncertainty of our $z \approx 10$ candidate. The lowest luminosity point has been corrected for incompleteness. The ultraviolet luminosity functions^{1,9} at $z \approx 4$ (blue) and at $z \approx 7$ (magenta) are shown for comparison. The luminosity functions fitted here are of the form $\phi^* e^{-L/L^*} (L/L^*)^\alpha$ (see Fig. 2 legend). This analytic representation has recently been shown⁹ to fit well at $z \sim 7$ and later times. The present search results also allow us to estimate the value of L^* at $z \approx 10$ – assuming that the luminosity function at $z \approx 10$ has the same values of ϕ^* and $\alpha \approx -1.7$ as have been found to describe ultraviolet luminosity function results from $z \approx 7$ to $z \approx 4$ (refs 1, 2, 9, 27-29). Doing so allows us to constrain

the evolution in the luminosity function out to $z \approx 10$, nearly 500 Myr earlier than at $z \approx 6$ (and so halving the time difference between the first galaxies at $z \approx 15$ -20 and those seen at $z \approx 6$). We find L^* at $z \approx 10$ to be -18.3 ± 0.5 AB mag, or $L^* > -18.3$ in the limit of no detected sources – although obviously very uncertain, this is consistent with the evolution in the bright end of the ultraviolet luminosity function seen from $z \approx 7$ to $z \approx 4$ continuing to $z \approx 10$.

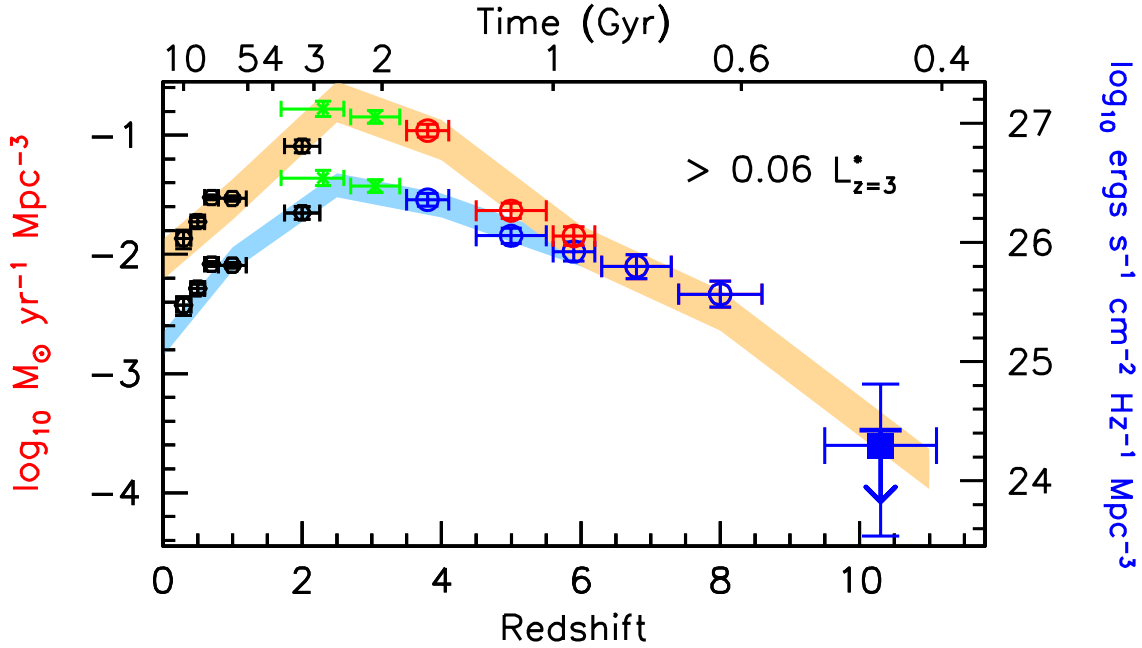


Figure 4. The luminosity density and star formation rate density in the Universe over 13.2 Gyr. The rest-frame continuum ultraviolet luminosity density (right axis, blue points) at $z \approx 10$, and the star formation rate density (left axis, red points) derived from the extinction-corrected luminosity density^{1,25}, are integrated down to the approximate magnitude limit $M_{AB} \approx -18$ ($0.06 L^*$) of our $z \approx 10$ J_{125} -dropout search. The conversion from ultraviolet luminosity to star formation rate assumes a Salpeter initial mass function. The upper horizontal axis gives the time after the Big Bang and the lower axis the redshift. As before, we assume that the ultraviolet luminosity function has the same faint-end slope (and normalization) as at $z \approx 6$ and $z \approx 7$. The star formation rate density ($1.9_{-1.5}^{+4.4} \times 10^{24} M_{\odot} \text{ yr}^{-1} \text{ Mpc}^{-3}$) from the contamination-corrected sample is shown at $z \approx 10$ from the current J_{125} -dropout search, as is the 1σ upper limit ($< 3 \times 10^{24} M_{\odot} \text{ yr}^{-1} \text{ Mpc}^{-3}$) if we assume no $z \approx 10$ sources are detected. All error bars are 1σ . Also included here are the recent star formation rate determinations at $z \approx 7$ and $z \approx 8$ from our HUDF09 WFC3/IR z_{850} -dropout and Y_{105} -dropout searches⁹, and from the literature at $z < 4$ (green and black points: refs 27, 30) and at $z \approx 4$ -6 (ref. 1). The dust corrections at $z \approx 4$ are based on the estimated ultraviolet-continuum slopes β , and are already negligible by $z \approx 7$ (refs 2, 3, 25). There is no evidence for any substantial change in the star formation rate density trends established at lower redshift.

Supplementary Information for Nature Letter
Searches and limits for $z \sim 10$ galaxies in the HST HUDF09 Data
R.J. Bouwens, G.D. Illingworth and the HUDF09 Team

1. General Outline

Here we describe our organizational plan for the Supplementary Information to our paper on searches for $z \sim 10$ galaxies in the ultra-deep HUDF09 WFC3/IR data. In the main section (§1-§11), we present an analysis of the $z \sim 10$ and $z \gtrsim 8.2$ searches we performed in the full two-year data set, as well as any conclusions derived on the basis of those searches. Included in the main section is a description of the observational data (§2), the procedure by which we construct source catalogs (§3), our $z \sim 10$ and $z \gtrsim 8.2$ searches (§4, §5), $z \sim 10$ searches in wider-area observations (§6), an assessment of possible contamination (§7), comparison of the selection from the full two-year data set to the first-year selection (§8), the expected number of high-redshift candidates in our selections (§9), the implications for high-redshift LFs (§10), and implications for the SFR density at $z \sim 10$ (§11).

In the Appendix, we will provide an assessment of the search we performed for $z \sim 10$ galaxies in the first-year HUDF data, where we reported three possible $z \sim 10$ candidates (arXiv:0912.4263). These sources have now been checked in the full two-year dataset, and found to have S/N that is too low to be credible candidates.

2. Observational Data

We make use of the ultra-deep two-year 4.7 arcmin² WFC3/IR observations over the HUDF from the HUDF09 program (GO 11563: PI Illingworth). We also make use of the wide-area 39.2 arcmin² WFC3/IR observations over the GOODS field from the Early Release Science (ERS) program (GO 11359: PI O’Connell) to better constrain the bright end of the $z \sim 10$ luminosity function. The ultra-deep WFC3/IR observations over the HUDF include 24 orbits, 34 orbits, and 53 orbits of data in the F105W, F125W, and F160W bands, respectively.

Our reductions of the ultra-deep WFC3/IR observations over the HUDF follow a very similar procedure to that used in our previous reductions of ultra-deep NICMOS observations²² or other deep near-IR data. The process begins with individual *flt* files requested from the archive. These frames had already been subject to bias correction, dark subtraction, flat-field correction, and cosmic ray rejection, so minimal additional calibrations were required. The *flt* files obtained from the archive should be reasonably well calibrated, given that the on-the-fly pipeline processing by STScI already takes advantage of darks and flat fields constructed from on-orbit data (the *flt* frames available shortly after launch were based upon test data taken while still on the ground).

To improve the pixel-by-pixel S/N (and correct for any imperfections in the flats or darks), we median stacked all of the observations in the F105W, F125W, and F160W bands to create supermedian frames – which were subsequently subtracted from the individual images. Compact, bright point-like sources are then identified in each WFC3/IR image and in the ACS HUDF data. These source lists were used to align the WFC3/IR images with the ACS HUDF data²⁶ using our *superalign* software.³¹ A description of our reductions of the ultra-deep first-epoch WFC3/IR observations over the HUDF is already included in Oesch et al.² and Bouwens et al.³

The WFC3/IR observations were then drizzled onto the HUDF frame using the *multidrizzle* software³² while clipping 4σ outliers. As a result of this clipping procedure, small artifacts in individual exposures – such as hot pixels – will not significantly affect our reductions. We attempted to mask out pixels on the WFC3/IR camera that were affected by source persistence. This masking was performed by remapping our initial reductions of the data (or more precisely blotting median stacks of the data) back to the original frames, subtracting them from the original frames, coadding these subtracted frames for all exposures within a visit, smoothing, and then flagging all pixels above a 3σ threshold. This together with our dither strategy and CR clipping procedure ensures that our final reductions are not significantly affected by source persistence.

To further optimize the pixel-by-pixel S/N in our reductions (ensuring they were of the highest quality), we repeated our median stacks of the exposures in each band – but now masking out the sources apparent in our final stacks (rather than just those apparent in the individual exposures). We then subtracted these supermedian images off of each of the individual exposures and drizzled the data together to generate our final reductions. The WFC3/IR Y_{105} , J_{125} , and H_{160} data over the HUDF09 reach to 5σ depths of 29.6, 29.9, and 29.8, respectively, in $0.35''$ -diameter apertures (no correction is made to these magnitudes to account for the light in sources outside these apertures). These depths are estimated from measurements of the RMS fluctuations in the data itself using apertures of the same radii. These apertures are placed in blank regions of the data to avoid obvious sources. As a result, the noise is determined directly from the data and so any correlations in the noise are implicitly included in the estimated depths. For our selection, we are using smaller $0.26''$ -diameter apertures than for our estimated depths. This ensures that our S/N measurements for individual sources are less sensitive to uncertainties in the estimated sky levels.

For the ACS observations over the HUDF, we simply make use of the v1.0 ACS reductions.²⁶ The ACS/WFC B_{435} , V_{606} , i_{775} , and z_{850} -band optical data reach to 29.7, 30.1, 29.9, and 29.4 AB mag, respectively (5σ : $0.35''$ -diameter apertures). The FWHMs of the PSFs are $\sim 0.10''$ and $\sim 0.16''$ in the ACS $BViZ$ and WFC3/IR YJH observations, respectively.

Our reductions of the WFC3/IR observations over the ERS fields were performed in a very similar manner to our HUDF09 reductions. Those observations reach to 27.9, 28.4, and 28.1 AB mag in the Y_{098} , J_{125} , and H_{160} bands, respectively (5σ : $0.35''$ -diameter aperture).⁹ The ACS/WFC B_{435} , V_{606} , i_{775} , and z_{850} -band optical data are available from the ACS GOODS program³³ and various SNe search and follow-up programs.³⁴ Our reductions of these data^{1,35} are similar to the

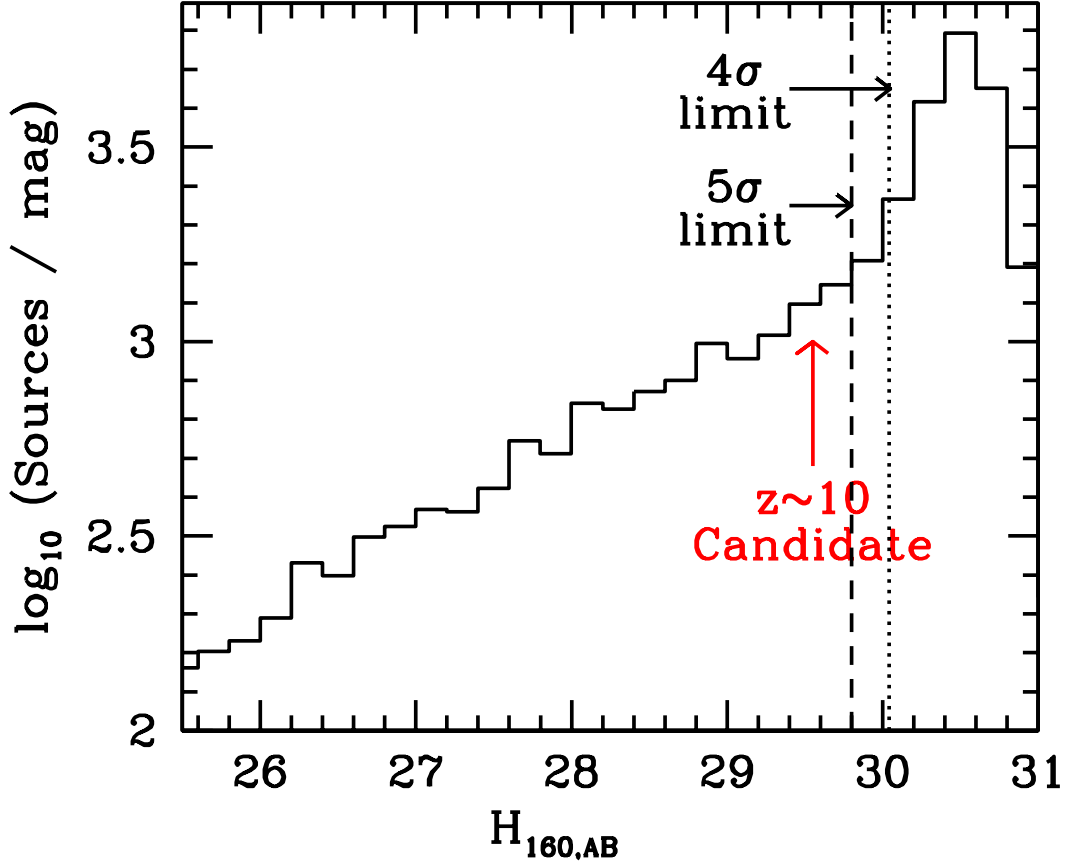


Fig. 1.— Number of sources per unit magnitude as a function of the H_{160} -band magnitude (measured in $0.35''$ -diameter) in our source catalogs. No correction for flux outside this aperture and on the wings of the PSF have been made, to compare with our 5σ limits (29.8 AB mag) quoted in the same manner and shown here with a dotted vertical line along with the 4σ limit. Our sole $z \sim 10$ J_{125} -dropout candidate is a $\gtrsim 5.4\sigma$ source ($0.26''$ -diameter aperture: but is $\sim 5.8\sigma$ in the aperture used for the magnitudes plotted in the figure) and is $\gtrsim 1.0$ mag brighter than the faintest sources in our catalogs (which are only $\sim 3\sigma$, and so excluded in our final selection).

GOODS v2.0 reductions, but reach ~ 0.1 - 0.3 mag deeper in the z_{850} band (due to the inclusion of the SNe follow-up data³³). These reductions reach to 28.2, 28.5, 28.0, and 28.0 AB mag in the B_{435} , V_{606} , i_{775} , and z_{850} bands, respectively (5σ : $0.35''$ -diameter apertures).

3. Source Catalogues

Our procedure for doing object detection and photometry is essentially identical to that performed in many previous analyses by our team.^{1,22,25,36} We provide a brief summary here. The SExtractor software³⁷ is used for object detection and photometry. Object detection is performed using the H_{160} -band image. The ACS optical images are smoothed to match the WFC3/IR images, and colors are measured in small scalable apertures (using a Kron³⁸ factor of 1.2). (A scalable aperture is the area in a two-dimensional ellipse where the major axis, minor axis, and orientation angle are set equal to some multiple of the first moments of light in an object.) Fluxes in these small scalable apertures are corrected to total magnitudes, considering the flux in a larger scalable aperture (Kron factor of 2.5). This latter correction is made using the H_{160} -band image. Finally, a correction is made for light outside this large scalable aperture using the encircled energies tabulated for point sources in the WFC3/IR F160W band (http://www.stsci.edu/hst/wfc3/documents/handbooks/currentIHB/c07_ir7.html).

4. J_{125} -dropout Selection

We search for high redshift galaxies at $z \sim 10$, utilizing J_{125} -dropout selection criteria. These selection criteria should permit us to identify candidate $z \sim 10$ star-forming galaxies in the ultra-deep WFC3/IR data, should they be brighter than 29.5 AB mag ($>0.06 L_{z=3}^*$: where this limit implicitly includes a fairly minimal correction for light on the PSF wings). Figure S1 shows the number of sources we find in the WFC3/IR HUDF09 observations over the HUDF versus H_{160} -band magnitude.

For our selection criteria, we require candidates to have $J_{125} - H_{160}$ colors redder than 1.2 AB mag, to be undetected ($< 2\sigma$) in all imaging observations blueward of the J_{125} band, and to be detected at $\gtrsim 5\sigma$ detection in the H_{160} -band. This significance measurement in the H_{160} band is made in a small ($0.26''$ -diameter) circular aperture to ensure the result is more robust. Significance measurements in scalable apertures, with variable position angles and axis ratios, are more susceptible to biases, since the apertures chosen to evaluate the significance of sources are affected by noise within those sources themselves.

In addition, our J_{125} -dropout candidates must not be detected at $>1.5\sigma$ in more than one band blueward of the J_{125} band. Finally, to ensure that the optical imaging data are used to maximal effect to reject low-redshift interlopers, we additionally require that candidates have a χ^2 value < 2.5

in the $B_{435}V_{606}i_{775}z_{850}Y_{105}$ -band χ^2 image.³⁹ The χ^2 image is equal to $\sum_k SGN(I_k)(I_k(x, y)/N_k)^2$. $I_k(x, y)$ is the intensity of image I_k at pixel (x, y) , $SGN(I_k)$ is 1 if $I_k > 0$ and -1 if $I_k < 0$, and N_k is the RMS noise on that image. In the definition of χ^2 , the index k runs over all the relevant images (i.e., those blueward of the dropout band).

All of these requirements place very strong limits on the detected optical light for our $z \sim 10$ candidates and provide strong discrimination against contamination by low-redshift sources. While we might occasionally reject some bona-fide $z \sim 10$ candidates utilizing this procedure, our primary objective with this selection is to make it as clean as possible (given the inherent difficulty in selecting $z \sim 10$ galaxies at modest S/N levels). We stress that the volume densities we compute for $z \sim 10$ candidates will not be affected by this choice, since we also impose these same selection criteria when computing the selection volumes.

We identified only one source which satisfied these stringent criteria over the ultra-deep HUDF09 WFC3/IR data. This source is listed in Table S1 and is shown in Figure 1 of the main text. This candidate is detected at 5.4σ in the $0.26''$ -diameter aperture used for selection and has an apparent magnitude of 28.9 ± 0.2 mag. The candidate has a significance of 5.8σ in a larger $0.35''$ -diameter aperture.¹ The candidate was not present in two previous catalogs of $z \sim 10$ candidates over the WFC3/IR HUDF09 observations. It falls just below 5σ at 4.7σ in these previous catalogs (which were based on only 50% of the two-year data set).

Our second and third best candidates are $<5\sigma$ detections in the H_{160} -band and hence do not make it into our election. Our second best candidate UDFj-38116243 (03:32:38.11, $-27:46:24.3$) is detected at 4.9σ in the two-year observations, while our third best candidate UDFj-39537198 (03:32:39.54, $-27:47:19.9$) is detected at 4.0σ . It is interesting that our second best candidate UDFj-38116243 in the full two-year observations was our most significant candidate in the first-year observations. However it is striking that its S/N is dramatically lower in the second year observations (just 1.3σ) and so it is not a particularly credible source. It is discussed further in Appendix A. It is also noteworthy that our best candidate UDFj-39537198 (the only source in our current $z \sim 10$ sample) has both a substantially higher significance level than the next most significant candidates, and a much more uniform distribution of detection significances with time (see Figure S2 and §7). As we will argue in §7, this strongly suggests that UDFj-39546284 corresponds to a real galaxy and is not spurious.

To ascertain the nature of the new single J_{125} -dropout candidate, we also examined the available IRAC 3.6μ and 4.5μ data. These data reach to $\lesssim 27.7$ AB mag and $\lesssim 27.1$ mag, respectively, at 1σ . After carefully modelling and subtracting the IRAC flux from nearby neighbors,⁴⁰ no significant ($>2\sigma$ or $>1\sigma$) 3.6μ or 4.5μ detections are found in the IRAC data (Figure 1 of the main paper). This implies a $H_{160} - 3.6\mu$ color of <1.2 mag (1σ limit) – which is more consistent with

¹To be conservative we do not use the larger-aperture significance levels for our selection (since the larger aperture measurements can be more affected by uncertainties in the background level).

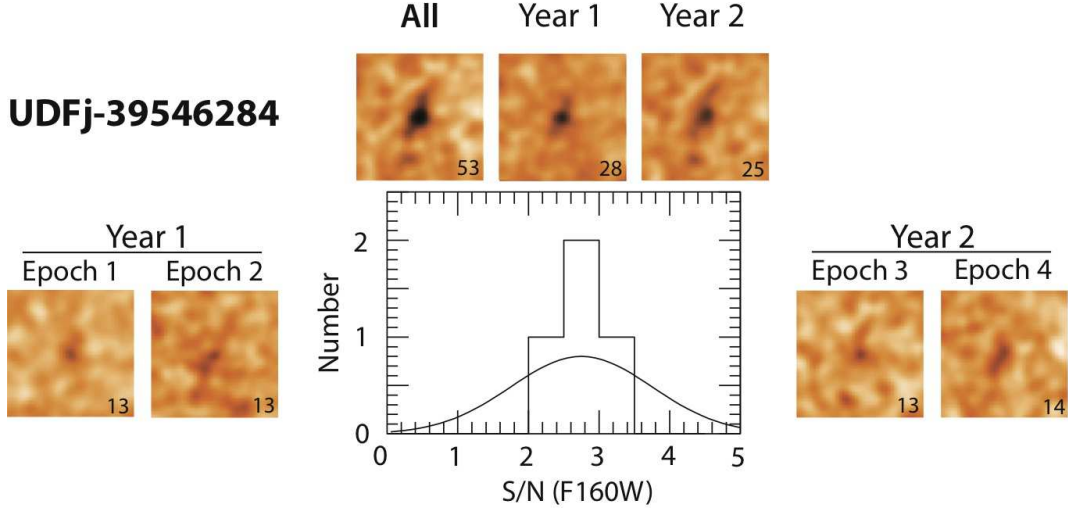


Fig. 2.— Images of the single $z \sim 10$ J_{125} -dropout candidate UDFj-39546284 from various subsets of the ultra-deep WFC3/IR H_{160} -band observations over the HUDF (53 orbits in total), including 13-orbit subsets of the ultra-deep in the lower panels. The distribution of the S/N levels for our $z \sim 10$ candidate in the 13-orbit subsets of the H_{160} -band observations is also shown. This S/N distribution for these 13-orbit subsets is expected to be approximately normal, with a mean of $5.4\sigma/4^{0.5} \sim 2.7\sigma$ and standard deviation of 1 (solid line). The observed S/N distribution is in reasonable agreement with expectations (see also Figure S6). The number of orbits of observations for each subset is given in the lower right corner. Two orbits from the first-year observations are incorporated into the epoch 3 observations to ensure each epoch had approximately the same 13-orbit exposure time. Note that our single J_{125} -dropout candidate is visible at $\geq 2\sigma$ in all four 13-orbit subsets of the data and that the S/N of the object in each subset is consistent with the expected value of 2.7σ .

this source being a star-forming galaxy at $z \sim 10$ than an evolved or dusty galaxy at $z \sim 2$.

5. Y_{105} -dropout Selection

We also carried out a search for galaxies at redshifts somewhat higher than 8 (comparable to or higher than the redshift of the gamma-ray burst source found^{10,11} at $z \sim 8.2$). For this, we require sources to have a very strong $Y_{105} - J_{125} > 1.5$ breaks (see Figure S3), to be undetected ($< 2\sigma$) in all bands $BViz$ blueward of the break, and to be detected at $\gtrsim 5.5\sigma$ in the J_{125} -band to ensure they correspond to real sources. This Y_{105} -dropout selection criterion is more stringent than what we applied in our earlier searches over the ultra-deep HUDF WFC3/IR data^{3,9} and identifies galaxies in the range $z \sim 8.2$ - 8.8 , with a mean redshift of $z \sim 8.5$ (see Figure 2 of the main text).

We identified three sources which satisfied these selection criteria. These sources are listed in Table S1 and shown in Figure S4. Two of our three candidates (the brightest ones) were already presented in the Bouwens et al.³ Y_{105} -dropout selection, the McLure et al.⁴ $z \sim 6$ - 9 search, the Bunker et al.⁵ Y_{105} -dropout selection, the Yan et al.⁶ Y_{105} -dropout sample, and the Finkelstein et al.⁷ $z \sim 6.3$ - 8.6 sample.

Table 1. Our single $z\sim 10$ J_{125} -dropout candidate and three $z\sim 8.5-9$ Y_{105} -dropout candidates identified over the ultra-deep HUDF09 WFC3/IR observations over the HUDF

Object ID	R.A.	Dec	H_{160}^a	$Y_{105} - J_{125}^b$	$J_{125} - H_{160}$	r_{hl}^c	z_{est}^d
UDFj-39546284	03:32:39.54	-27:46:28.4	28.92 ± 0.18	—	>2.0	$0.13''$	10.3
UDFy-38135539	03:32:38.13	-27:45:53.9	27.80 ± 0.08	1.8 ± 0.7	0.2 ± 0.1	$0.18''$	8.7
UDFy-37796000	03:32:37.79	-27:46:00.0	28.01 ± 0.11	>2.3	-0.1 ± 0.1	$0.19''$	8.5
UDFy-33436598	03:32:33.43	-27:46:59.8	28.93 ± 0.18	>1.7	0.0 ± 0.2	$0.16''$	8.6

^aThe magnitudes quoted here are based upon the light inside our large scalable apertures (and also include $\sim 0.2-0.3$ mag corrections for light on the wings of the PSF). As such, they are significantly brighter than those quoted for our candidates in smaller apertures (e.g., in Figure S1).

^bLower limits on the measured colors are the 1σ limits.

^cThe quoted half-light radii are as observed and are not corrected for the PSF. The half-light radius r_{hl} for the PSF is $0.09''$.

^dEstimated redshift. See Figure 2 of the main paper for the redshift distributions

6. J_{125} -dropout selection over the Early Release Science observations

To constrain the volume density of sources at the bright end of $z \sim 10$ LF, we also conducted a search for $z \sim 10$ J_{125} -dropout candidates over the wide-area ERS observations. The ERS observations cover $\sim 10\times$ as much area as probed by our ultra-deep WFC3/IR observations over the HUDF. This large area is very valuable for constraining the volume density of the likely intrinsically very rare sources at the bright end of the $z \sim 10$ LF.

Both our catalog construction procedure and selection criteria remain the same as what we used for the ultra-deep HUDF09 field. We find no candidates with $J_{125} - H_{160}$ colors > 1.2 and optical non-detections over the ERS observations. The only sources that satisfy those criteria were also quite bright at 5.8μ and 8.0μ , and hence were likely $z \sim 2-3$ dusty galaxies (having $H_{160} - 5.8\mu$ colors redder than ~ 2).

7. Possible Contamination

Contamination from Spurious Sources: Perhaps the most important issue to examine in assessing the present J_{125} -dropout selection is determining whether our candidate is real or whether it could be due to random fluctuations in the noise (i.e., spurious). Since our candidate is only detected in a single passband at $\sim 5.4\sigma$, one must consider the possibility that it could be spurious.

Contamination from Spurious Sources: Noise Distribution: To determine the probability that our candidate could be spurious, we first examine the noise distribution in our ultra-deep WFC3/IR images. This is important since it will allow us to quantify the extent to which noise in WFC3/IR images has non-Gaussian characteristics and therefore might allow for $\gtrsim 5\sigma$ noise fluctuations (i.e., outliers) simply by chance.

We start by examining the noise distribution in the J_{125} -band image, since we would not expect many faint sources with emission in the J_{125} -band alone and not in the other frames. The distribution of flux values in 3 pixel-by-3 pixel boxcar smoothed regions is shown in the upper panel of Figure S5 after masking out all those regions which show $\geq 1.5\sigma$ detections in a coaddition of the optical, Y_{105} , and H_{160} images. A similar noise distribution is shown in the lower panel for fluctuations in the H_{160} -band, after masking out those regions detected in the other bands. Overall, the noise distributions appear to be approximately Gaussian to the extent that it can be tested with our data and only show minor deviations. This suggests that apparent 5σ events are indeed significant at approximately 5σ , and therefore the 5.4σ J_{125} -dropout in our sample is not likely a chance noise fluctuation.

Contamination from Spurious Sources: Splitting the Data: Another procedure for testing the reality of our J_{125} -dropout candidate is to split the H_{160} -band data into four independent subsets of 13 orbits (representing $\sim 25\%$ of the total data set) and evaluate the significance of this candidate in

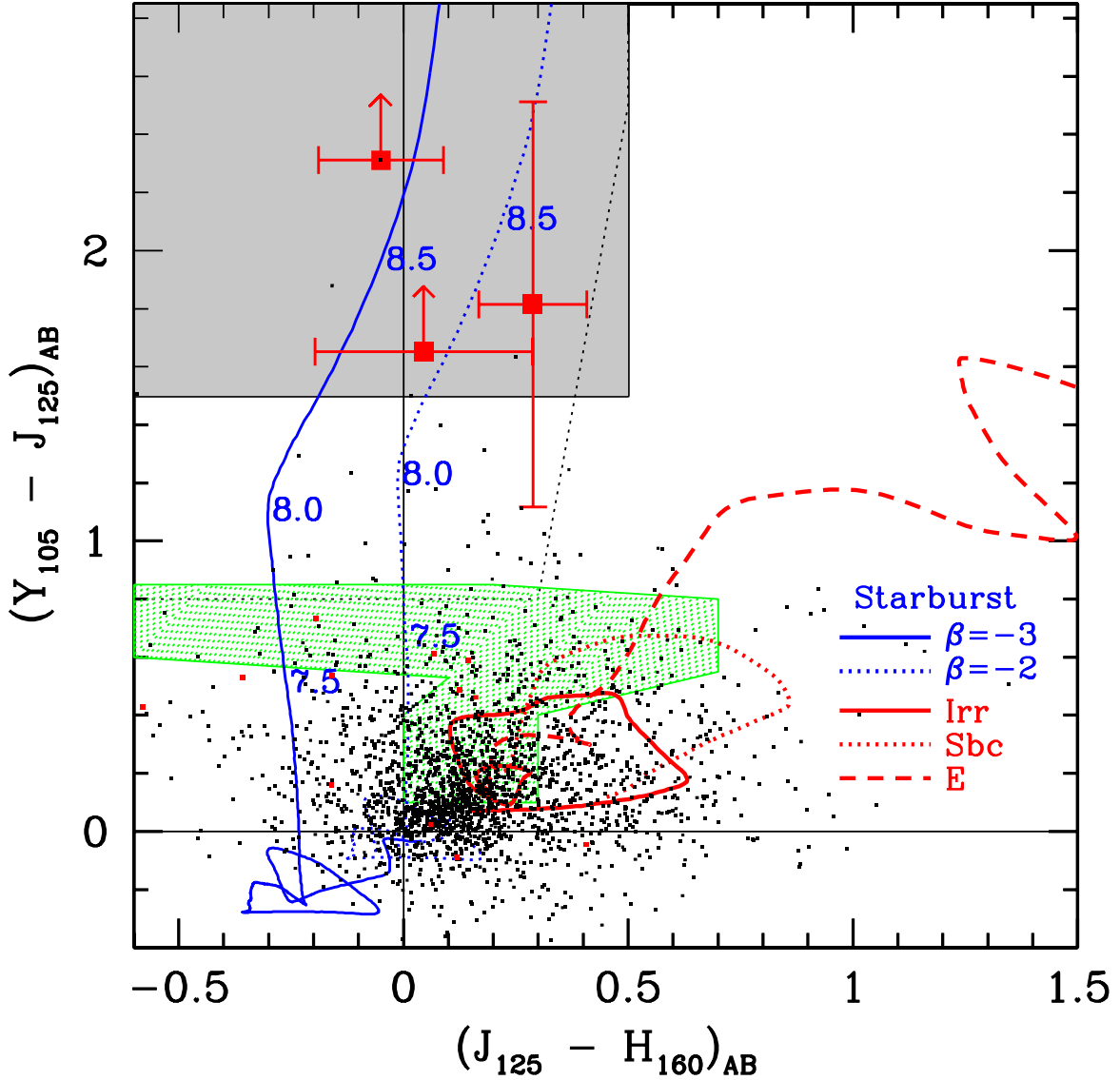


Fig. 3.— $Y_{105} - J_{125} / J_{125} - H_{160}$ two color selection used to identify $z \gtrsim 8.2$ Y_{105} -dropout galaxies. For context, the colors of star-forming galaxies with different UV -continuum slopes β of -3 , -2 versus redshift are also shown. Also presented are the colors of low-redshift galaxy SEDs⁴¹ over the redshift range $z \sim 0-2$. The Y_{105} -dropout selection window is presented in gray. The objective of the current Y_{105} -dropout selection is to identify those Y_{105} -dropouts from the HUDF with the highest redshifts. The current sample of Y_{105} -dropouts is nonetheless a subset of the Y_{105} -dropouts identified in the Bouwens et al.³ and Bouwens et al.⁹ Y_{105} -dropout selections (the dotted black lines show the selection used by Bouwens et al.³). The hatched green region indicates the region in color space we would expect L, T dwarfs to lie.⁴²

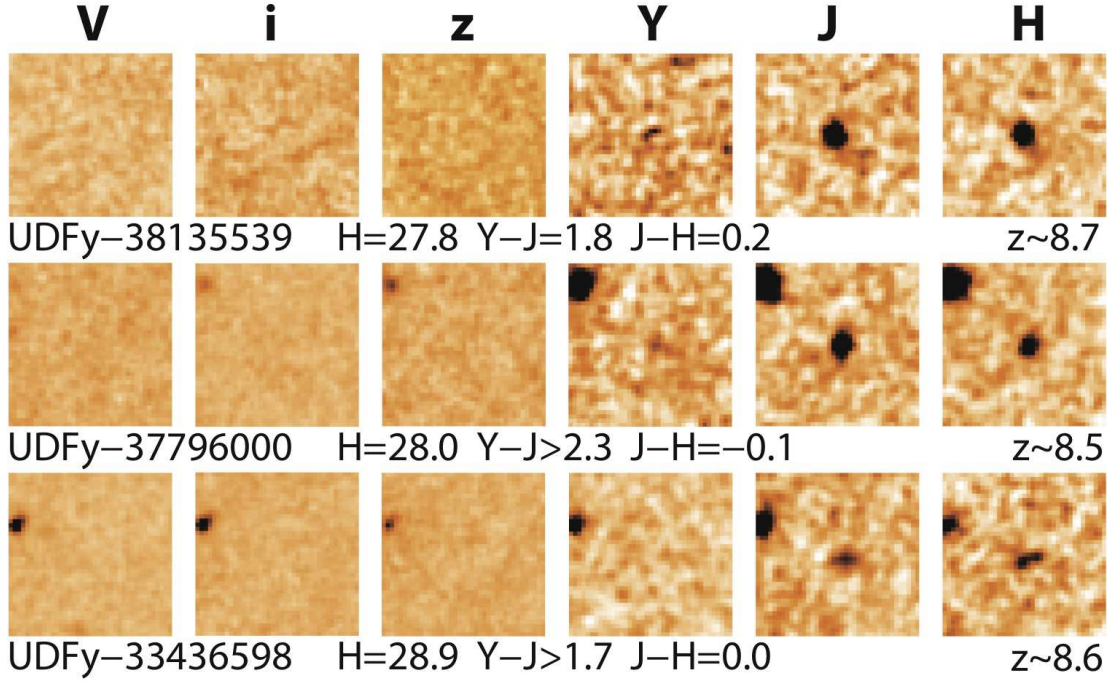


Fig. 4.— $V_{606}i_{775}z_{850}Y_{105}J_{125}H_{160}$ image cutouts of three $z \sim 8.5$ Y_{105} -dropout galaxy candidates we identified in the ultra-deep HUDF WFC3/IR observations (§5). None of the candidates are detected in the deep ACS $BVi z$ observations. The candidate UDFy-38135539 has a tentative spectroscopic confirmation at $z \sim 8.6$.¹⁴ Other properties of the candidates are given in Table S1. Each cutout is $2.4'' \times 2.4''$ on a side and with North up.

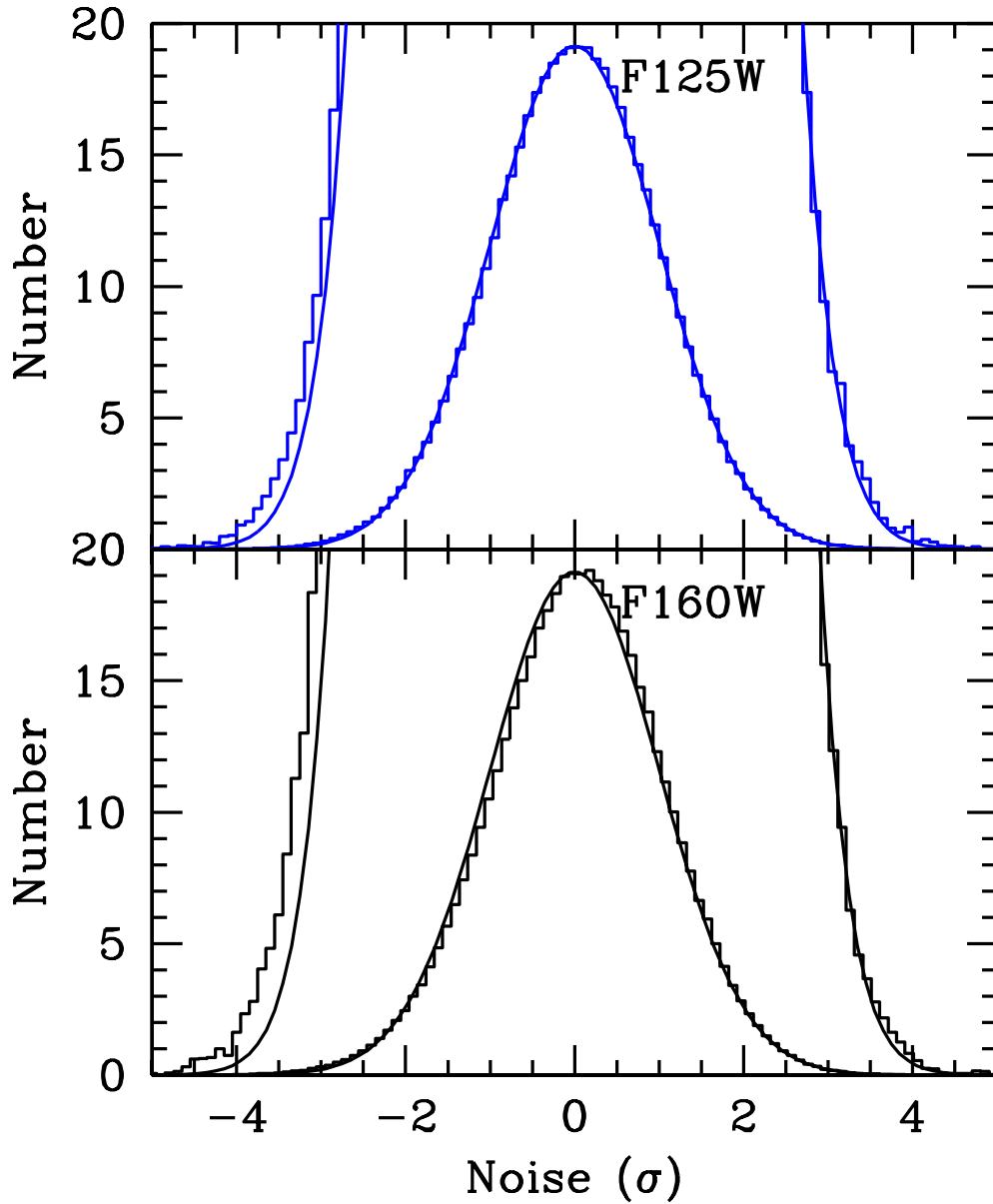


Fig. 5.— Observed distribution of noise fluctuations in 3 pixel by 3 pixel regions in the F125W and F160W band observations (histograms: upper and lower panels, respectively). The solid line shows the model noise distribution, for perfectly Gaussian noise. While the observed distribution of fluctuations does show slight skewness, this distribution is almost perfectly Gaussian out to significance levels of $\sim 3.5\sigma$. The noise distribution for positive fluctuations appears to only exceed that expected from normal statistics, by less than a factor of 2.

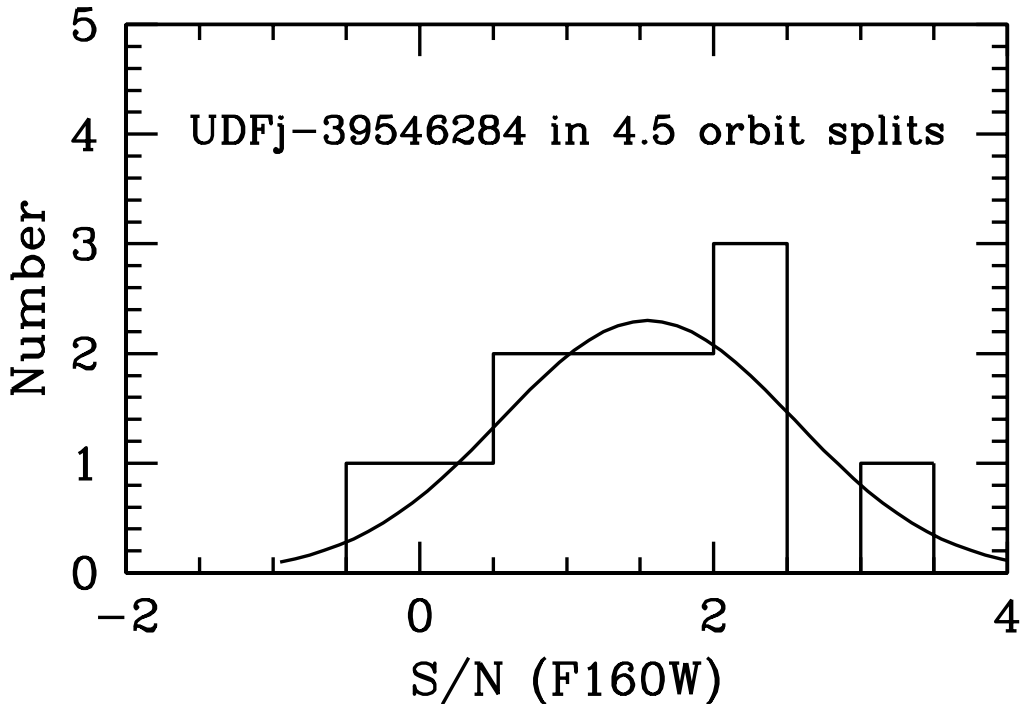


Fig. 6.— The distribution of S/N levels for our $z \sim 10$ candidate in 12 independent 4.5-orbit splits of the H_{160} -band observations (53 orbits in total). Because 53 orbits cannot be split evenly into 12 4.5-orbit subsets, one split only included 3.5 orbits. This distribution appears to be a good fit to a normal distribution with a mean of 1.6σ and standard deviation of 1σ . A mean of 1.6σ is exactly what one would predict based upon a scaling of the S/N with the square root of the number of exposures, i.e., $5.4\sigma/12^{1/2} \sim 1.6\sigma$. The general agreement of the S/N distribution for our J_{125} -dropout candidate with that expected for Gaussian noise suggests that this candidate is not spurious.

each subset. The four ~ 13 -orbit splits are shown in Figure S2, and it is evident that our candidate is significant in each split. In a $0.26''$ -diameter aperture, it is significant at 3.4σ , 2.7σ , 2.3σ , and 2.7σ , with a mean of 2.8σ . The significance is thus $\geq 2.3\sigma$ in all four splits (see Figure S6). Since 2.3σ events occur with probability $\lesssim 1\%$ and there are only $\sim (133''/0.2'')^2 \sim 700^2$ independent resolution elements over the WFC3/IR HUDF in which such sources could be found, there is $\lesssim 1\%$ chance that this event would be found at random. A modification of this test to consider even smaller 4.5-orbit subsets of the data provides a more rigorous assessment of the robustness of our candidate against non-Gaussian fluctuations. The distribution of significance levels for our candidate in 4.5-orbit splits is consistent with a normal distribution with a mean of 1.6σ and scatter of 1σ (Figure S6).

A slight variation of the above tests would be to see if the candidate were amongst the most significant candidates in the first and second year observations. We would not expect there to be a highly significant candidate at approximately the same position in both the first and second year observations if it were spurious. Constructing J_{125} -dropout catalogs from the first and second year observations and extending our selection down to 3σ , we found a $\geq 3\sigma$ J_{125} -dropout candidate in the second-year observations within $0.06''$ of a similar $\geq 3\sigma$ J_{125} -dropout candidate in the first-year observations. This candidate was the 2nd most significant J_{125} -dropout candidate in the first year observations and the 10th most significant in the second. The probability that one of the ten most significant candidates in both the first and second year observations would occur within $0.06''$ of each other is $\sim 10^2(\pi(0.06'')^2)/(133'')^2 \sim 0.01\%$.

Contamination from Spurious Sources: Negative Image Test: Two other procedures for assessing the probability that our candidate might be spurious are the “negative image” test³⁵ and a test where we look for similar 5σ detections (single or multiple band) in bluer filters. The rationale for using the negative images is that the noise properties are fairly symmetric in the positive and negative directions (see Figure S5), and therefore a search for J_{125} -dropout candidates in negative images allows us to assess the relevance of spurious sources to our selection. A search for J_{125} -dropout candidates on the negative H_{160} -band images yielded no candidates. Nonetheless, we do note the presence of a source just below our selection threshold (at 4.8σ : but no others above 4.4σ). Though it is difficult to calculate precisely how much more significant our 5.4σ J_{125} -dropout candidate is than this 4.8σ spurious source, for Gaussian statistics it is approximately $\sim 20\times$ more likely. This again suggests our selection is probably free of contamination from spurious sources.

Contamination from Spurious Sources: $Y_{105} + J_{125}$ /single-band J_{125} test: A search for sources which were 5σ detections in a 53-orbit $Y_{105} + J_{125}$ image (the two-bands are combined to construct an image with an equivalent number of exposures to our two-year H_{160} -band stack and hence similar noise statistics) revealed no 5σ sources with $H_{160} - Y_{105}/J_{125}$ colors > 1.2 not seen in the H_{160} -band. The most significant source in the $Y_{105} + J_{125}$ image was 4.5σ . Again this suggests that our sole $z \sim 10$ candidate is not spurious. However, we do note that we do find a 5.1σ single-band detection if we examine only the 34-orbit J_{125} -band (and not include the Y_{105} -band in the stack). While the existence of such a source in the J_{125} -band data could indicate that non-Gaussianity is

still important for ~ 30 -orbit exposures with WFC3/IR,² it seems clear that non-Gaussianity will be less important for our 53-orbit H_{160} -band stack.

Finally, we remark that we identified our sole J_{125} -dropout candidate as the most promising candidate shortly after the second-year WFC3/IR H_{160} -band observations over the HUDF began and when there were 15 orbits of H_{160} -band observations remaining. The subsequent observations were therefore a test of the reality of the candidate. As is evident in Figure S2, the source is significant at $\geq 2.5\sigma$ in the observations taken after this point – which would occur at only 1% probability if the source were spurious.

Most of the above tests suggest contamination from spurious sources at $\sim 1\%$ probability – though the results from the negative image test and $Y_{105} + J_{125}/J_{125}$ -band tests suggest a contamination rate as high as 10%. To be conservative, we will assume that the contamination rate from spurious sources in our selection is 10%, or ~ 0.1 . However, we stress that such formal analyses should be treated with caution as unknown effects could be present in the data.

Contamination from Red Low-Redshift Galaxies: An equally important concern for the present J_{125} -dropout selection is contamination from compact, low-surface brightness, low-redshift, very red sources (typically because of age or dust). It is plausible that such sources could satisfy our J_{125} -dropout selection criteria, with $J_{125} - H_{160}$ colors redder than 1.2 and showing very little flux in the ultra-deep optical data. Obviously, we might expect such sources to be somewhat brighter at redder wavelengths, and so the IRAC data provide us with a way of constraining this possibility. As we noted in the previous section, each of our candidates is undetected in the 3.6μ band, allowing us to set a $H_{160} - 3.6\mu < 1.2$ limit on its color blueward of the $J_{125} - H_{160}$ break – providing some evidence that J_{125} -dropouts in our selection are not just red galaxies at $z \sim 2$.

An independent way of examining whether lower-redshift red galaxies are a concern for our J_{125} -dropout selection is performing an analogous selection for $z \sim 8$ Y_{105} -dropouts – assuming that no H_{160} -band observations are available. We therefore select Y_{105} -dropouts using two criteria: being undetected in the optical data and satisfying a single color $Y_{105} - J_{125} > 1.2$ cut (and no $J - H$ criterion). In performing this experiment, we only remove sources that are bright enough in the optical that they would be detected if the source had the same H_{160} -band magnitudes as our J_{125} -dropout candidates (which are typically ~ 0.5 mag fainter). We identify exactly the same sources in this Y_{105} -dropout selection as we would select also including a $J_{125} - H_{160} < 0.5$ selection on the $J - H$ color (8 sources in total from the HUDF09 and HUDF09-2⁹ fields). This suggests that our lack of ultra-deep imaging data redward of the H_{160} -band does not substantially add to the contamination.

This test demonstrates how powerful an optical non-detection criterion combined with a strong

²It is possible that non-Gaussianity may explain the existence of UDFj-38116243, one of our J_{125} -dropout candidates and apparent 5σ detection in the first-year data (see Appendix).

color break in broadband SED can be in identifying $z \geq 7$ galaxies, given the colors of faint sources in deep field data. It also suggests that other techniques that do not take advantage of information about the actual prevalence of sources with specific colors at faint magnitudes may actually overestimate the contamination rate for high redshift selections (e.g., “photometric redshift” techniques that compute $P(z)$ based upon χ^2 fits to various SED templates versus redshift).

This is a very powerful independent test that suggests our single-band approach is much more robust than it might first appear. The reason that such a selection is so useful is that the HUDF has such a variety of deep data in so many filters over a wide wavelength range to check for contamination.

Contamination from Photometric Scatter: Another possibly significant source of contamination for the current J_{125} -dropout selection are sources that satisfy our J_{125} -dropout criterion due to noise in the photometry. To assess this possibility, we considered each faint source in our H_{160} -band catalog in turn, randomly selected a source in H_{160} -band magnitude range 26.5 to 27.5 AB mag (taken to be representative of the color distribution at fainter magnitudes), rescaled their fluxes to match the fainter source in our H_{160} -band catalog, added noise, and finally reapplied our J_{125} -dropout selection criteria. Repeating this simulation many times, we found that ~ 0.1 contaminants per field satisfy our J_{125} -dropout criterion, simply as a result of noise. A detailed description of this procedure (but for z or Y dropouts) is discussed in Bouwens et al.⁹

Other Sources of Contamination: Other possible sources of contamination for our J_{125} -dropout includes transient sources like SNe or stars. Contamination by SNe seems extremely unlikely since the J_{125} and H_{160} observations were taken within 5 days of each other. Contamination by stars also seem rather implausible, since the source appears to be slightly resolved, and the only stars which are red enough to satisfy the $J_{125} - H_{160} > 1.2$ criterion are extreme carbon stars or Mira variables⁴⁴ – which would need to be located well outside our galaxy⁴⁵ given their luminosity.

Lastly, all of our candidates are sufficiently separated from extended foreground sources that they are unlikely subcomponents of these sources. A somewhat parallel concern in doing candidate selection near extended sources is that the detection significance of possible sources is enhanced by light from the extended wings. It seems quite probable that an independent selection of $z \sim 8$ -10 candidates⁶ may have been subject to significant contamination as a result of this issue (see arXiv:0912.4263 for a discussion of some problems with that selection).

Summary: The above simulations suggest we would find ~ 0.2 contaminants in the $z \sim 10$ J_{125} -dropout selection we perform over the HUDF09 observations: ~ 0.1 from spurious sources and ~ 0.1 from photometric scatter. This implies that 0.8 J_{125} -dropout candidates from our selection correspond to $z \sim 10$ galaxies. Of course, it is important to remember that such simulations can often have significant uncertainties and so we will also consider the case that we have not detected any $z \sim 10$ sources.

In the sections which follow, we will explore the implications (1) if 0.8 J_{125} -dropout candidates

here are at $z \sim 10$ and (2) if none are.

Contamination in Y_{105} -dropout selections: The only important source of contamination for Y_{105} -dropout selections seems to be sources that enter the selection as a result of photometric scatter (i.e. noise),³ and even for this source of contamination, we derive a contamination rate of $< 4\%$ from Monte-Carlo simulations.

8. Contrasting the current $z \sim 10$ selection with previous $z \sim 10$ selections

The second year of WFC3/IR observations do not provide significant support for the reality of the three candidates we initially identified in the first-year of observations, as we describe in Appendix A. Should we have more confidence in the sole $z \sim 10$ J_{125} -dropout candidate found in the full two-year observations than we had in our $z \sim 10$ candidates from the first-year observations? There are at least four reasons why we would argue the answer is *yes*.

First, we now have approximately twice the total exposure time to evaluate the reality of our $z \sim 10$ candidates, as we had previously. This additional exposure time is valuable since it provides for a very rigorous test of the reality of any possible candidates in our selection. In the present case, our sole $z \sim 10$ candidate shows up at $\geq 2.3\sigma$, with a mean of 2.8σ , in four ~ 13 -orbit splits (Figure S2) and with a mean of 1.6σ in 12 ~ 4.5 -orbit splits (Figure S6). The increased number of exposures also results in the candidate showing a higher significance level than any of the previous candidates. Lastly, the larger number of exposures results in the noise being more Gaussian in nature (from the well-known central limit theorem in statistics), making apparent high σ events genuinely more significant.

Second, we now use much more conservative selection criteria than we used in our first-year selection. The fixed apertures we utilize to evaluate the significance of sources are much less susceptible to biases than the scalable Kron-like apertures we had previously used, and only one of our previous three candidates would have been selected with such a procedure.

Third, our current $z \sim 10$ candidate is much more unique in terms of its overall significance levels than the candidates in the first-year selection. While there were a substantial number of sources between 4σ and 5σ in our first-year catalog, this contrasts with only two sources in that significance range here. This argues that the candidate is much more unique overall and it is not produced by sources scattering into our selection through noise.

Fourth, our current $z \sim 10$ candidate is found at magnitude levels much more consistent with it corresponding to bona-fide high-redshift galaxies than was the case for the first-year candidates. The reason for this is simple. Due to rapid changes in completeness, one expects candidates (in general) only to begin appearing a few tenths of the magnitude brightward of the selection limit since it is only at such magnitudes that the completeness will be high enough to observe high redshift galaxies in significant numbers. Below the selection limit, the number of bona-fide sources

becomes very small, first because the search is becoming seriously incomplete, and second because the contamination rate can increase rapidly. This is illustrated in the specific case of our $z \sim 10$ searches in Figure S1 and in Figure S7. The current $z \sim 10$ candidate is several tenths of a magnitude brighter relative to the selection limit (~ 29.8 AB mag in Figure 1) than were the three first-year candidates. This contrasts to the first year candidates in the same apertures which were actually $< 5\sigma$, and in two cases, much less (see Appendix A). The likelihood of contamination for the present $z \sim 10$ candidate (i.e., that the source is spurious) is therefore quite a bit smaller.

Together these improved tests and cross-checks, the higher significance and more robust S/N, all suggest that the new source is more likely to be a high-redshift galaxy – and, combined with the photometric data, a plausible $z \sim 10$ candidate. It is also reassuring that the surface density implied by this single candidate is close to what we would expect extrapolating from lower redshift (see §9 and Figure S7).

9. Expected Numbers

To provide a baseline for interpreting the number of high-redshift dropout candidates we have found over our search fields, we compare the present findings with what we might expect extrapolating lower-redshift results to $z \sim 10$ assuming no evolution.

We use a similar procedure as described in previous work^{3,21} to account for the many different selection effects (and incompleteness). We start by generating catalogues based upon the model LFs, creating realistic pixel-by-pixel simulations of the model sources, adding these simulated images to the actual ACS+WFC3/IR data, and then processing the images (and selecting the sources) in the same way as on the real data. By adding the model sources to the actual imaging data, we naturally account for the effect that foreground sources have on both the completeness of our dropout selections and the accuracy of our photometry.¹

The spatial profiles of the sources in the simulations are modelled using the pixel-by-pixel morphologies of similar-luminosity $z \sim 4$ B -dropout galaxies from the HUDF¹ scaled in size using the $(1+z)^{-1}$ size-redshift relation.^{46–48} The sources are also taken to have a UV -continuum slope distribution with a mean β equal to -3 and a scatter of 0.4 to match the observed trends with redshift.⁴⁹

For these no-evolution cases, we predict 23 and 12 J_{125} -dropouts over the HUDF and ERS fields using the $z \sim 6$ LF¹, 12 and 5 dropouts over the HUDF and ERS fields using the $z \sim 7$ LF⁹, and 9 and 2 dropouts over the HUDF and ERS fields using a $z \sim 8$ LF²² (consistent with the LF from Bouwens et al.⁹).

Since the LF does evolve quite markedly with redshift,²² we can make a much more realistic prediction for our $z \sim 10$ search results. We provide this prediction based upon the Bouwens et al.²² LF-fitting formula where the Schechter parameters are $M_{UV,AB} = -18.8$ and $\phi^* = 0.0016$

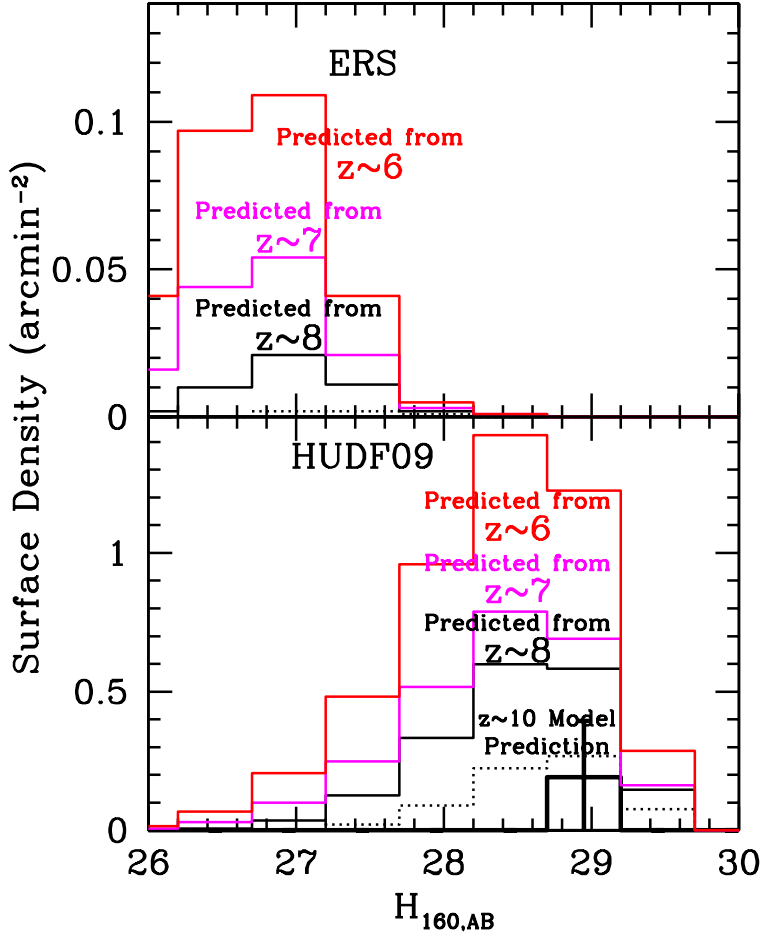


Fig. 7.— Observed surface densities of $z \sim 10$ J_{125} -dropout candidates (*histograms shown with thick black lines*) in the wide-area ERS observations (*top panel*) and ultra-deep HUDF09 observations (*bottom panel*). The observed surface densities have been corrected assuming $\sim 20\%$ contamination in the HUDF09 observations (see §7). For comparison, we have also plotted the expected surface densities of $z \sim 10$ J_{125} -dropout galaxies assuming no evolution in the UV LF¹ from $z \sim 6$ (*red histogram*), $z \sim 7$ (*magenta histogram*)⁹, and $z \sim 8$ (*black histogram*). The $z \sim 8$ LF we use for this no-evolution calculation adopts an $M^* \sim -19.5$, $\phi^* \sim 0.0014 \text{ Mpc}^{-3}$, and $\alpha = -1.74$ (obtained using the Bouwens et al.²² LF-fitting formula while keeping α fixed, but we note that it is consistent with observations⁹). We also show the predicted J_{125} -dropout surface densities adopting a $z \sim 10$ model LF (dotted histogram), with $M^* \sim -18.8$, $\phi^* \sim 0.0016 \text{ Mpc}^{-3}$, and $\alpha = -1.74$ (these parameters also come from the Bouwens et al.²² fitting formula but again keeping α fixed). The surface densities of $z \sim 10$ galaxies expected at ~ 29 AB mag are in good agreement with what we would infer if our single J_{125} -dropout candidate over the HUDF actually corresponds to a $z \sim 10$ galaxy. We refer the reader to e.g. Bouwens et al.^{3,9} for a discussion of the surface densities for $z \sim 8$ Y_{105} -dropout selections from the HUDF09 observations.

Mpc^{-3} . We fixed α to the same value -1.74 found at $z \sim 6$.¹ Based upon this LF, we predict 3 J_{125} -dropouts over the HUDF at $z \sim 10$ and 0.2 J_{125} -dropouts at $z \sim 10$ over the ERS observations.

The predicted J_{125} -dropout surface densities are presented in Figure S7 for the various UV LFs. Not surprisingly, significant numbers would be expected at brighter magnitudes based upon the UV LF at $z \sim 6$ and $z \sim 7$ if there is no evolution. However, we only detect a candidate $z \sim 10$ galaxy at the faint end of our deep HUDF09 search (i.e., $H_{160,AB} \sim 29$ for the HUDF09 observations). This again points towards significant evolution in the UV LF from $z \sim 10$ to $z \sim 7$. In the HUDF, the surface density of J_{125} -dropout candidates observed is comparable to that expected from an extrapolation of the UV LF to $z \sim 10$. It is remarkable that the Bouwens et al.²² LF fitting formula is plausibly consistent with the observations all the way out to $z \sim 10$.

We expect the field-to-field variance on the present J_{125} -dropout searches to be 39% and 40% in our HUDF09 and ERS searches, respectively – assuming a redshift selection window with width $\Delta z \sim 1.3$; a search area of 4.7 arcmin² and 39.2 arcmin², respectively; and bias factors of ~ 8 and ~ 12 , respectively. These bias factors correspond to source volume densities of $\sim 4 \times 10^{-4} \text{ Mpc}^{-3}$ and $\sim 3 \times 10^{-5} \text{ Mpc}^{-3}$, respectively, expected to be probed in our HUDF09 and ERS searches and were computed using the Trenti & Stiavelli²⁰ cosmic variance calculator. While large, these uncertainties are smaller than those expected, given the very small numbers (and thus large Poissonian errors).

The predicted redshift distributions for our J_{125} -dropout selection is given in Figure 2 of the main text. For this calculation, we assume that the UV LF at $z \sim 10$ has a $M_{UV}^* = -18.8$, $\alpha = -1.74$, and $\phi^* = 0.0016 \text{ Mpc}^{-3}$, i.e., using the Bouwens et al.²² LF fitting formula to extrapolate the $z \sim 4 - 7$ LF results to $z \sim 10$. The mean redshift for our $z \sim 10$ J_{125} -dropout selection is 10.3. Also presented in Figure 2 of the main text is the predicted redshift distribution of the present Y_{105} -dropout selection (assuming $M_{UV}^* = -19.5$, $\alpha = -1.74$, and $\phi^* = 0.0014 \text{ Mpc}^{-3}$) for each $z \sim 8.5$ candidate. The $J - H$ color for UDFy-38135539 is 0.4 mag redder than UDFy-37796000 and 0.3 mag redder than UDFy-33436598 – suggesting probable redshifts of 8.7, 8.5, and 8.6, respectively for the sources. While the latter redshift estimate is somewhat higher ($\Delta z \sim 0.2 - 0.3$) than the McLure et al.⁴ estimate for these two Y_{105} -dropouts, the present estimate adopts a somewhat bluer UV -continuum slope β distribution (as suggested by ref 49) than the likely SED templates used by McLure et al.⁴ for their redshift estimates.

10. Implications for the UV LF at $z \sim 10$

The depth and area of the present WFC3/IR observations have provided us with our best opportunity yet to find star-forming galaxies at $z \sim 10$, and therefore it is not surprising that we were able to find one plausible $z \sim 10$ J_{125} -dropout candidate.

The present search results permit us to significantly improve the constraints on the LF at $z \sim 10$. We begin by exploring stepwise constraints on the UV LF. The simulations described in §9

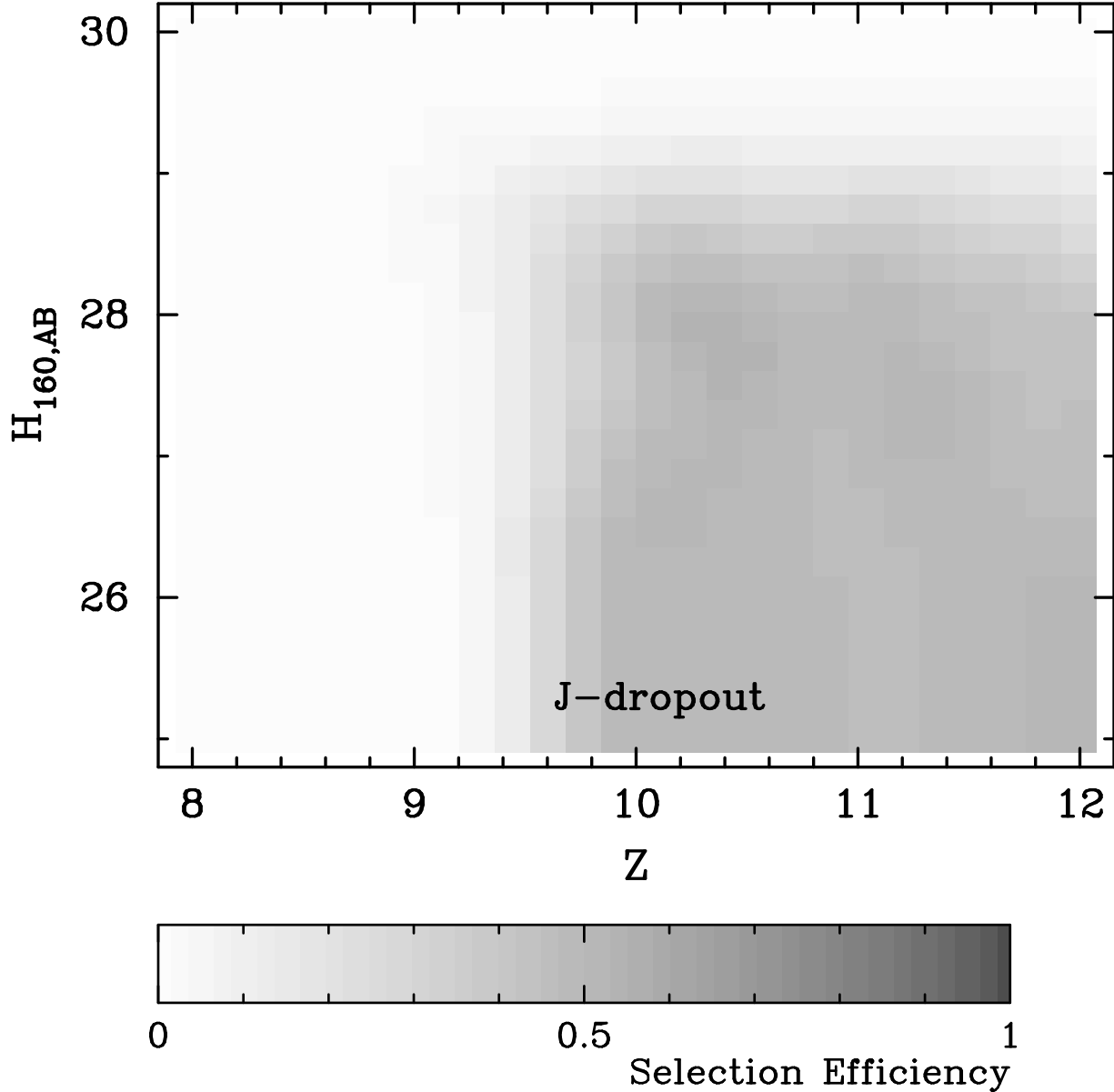


Fig. 8.— The efficiency with which we select star-forming galaxies versus redshift at specific apparent H_{160} -band magnitudes in the HUDF09 observations. These efficiencies are important for our LF constraints (§10) and were estimated by adding model galaxies with realistic colors and sizes to the actual observations and attempting to reselect them using the same procedure as we use on the observations (see §9). The reason the selection efficiency is lower than 100% is due to the area covered by both bright and faint foreground galaxies. The faint foreground galaxies make it difficult to register a clear “null” detection in the optical. We even lose $\sim 10\%$ of the area (even in empty regions) due to our requirement that χ^2 (from the BVizY data) < 2.5 and the fact that such a low χ^2 can be exceeded simply as a result of noise. Such a stringent optical non-detection criterion is required to keep the contamination low.

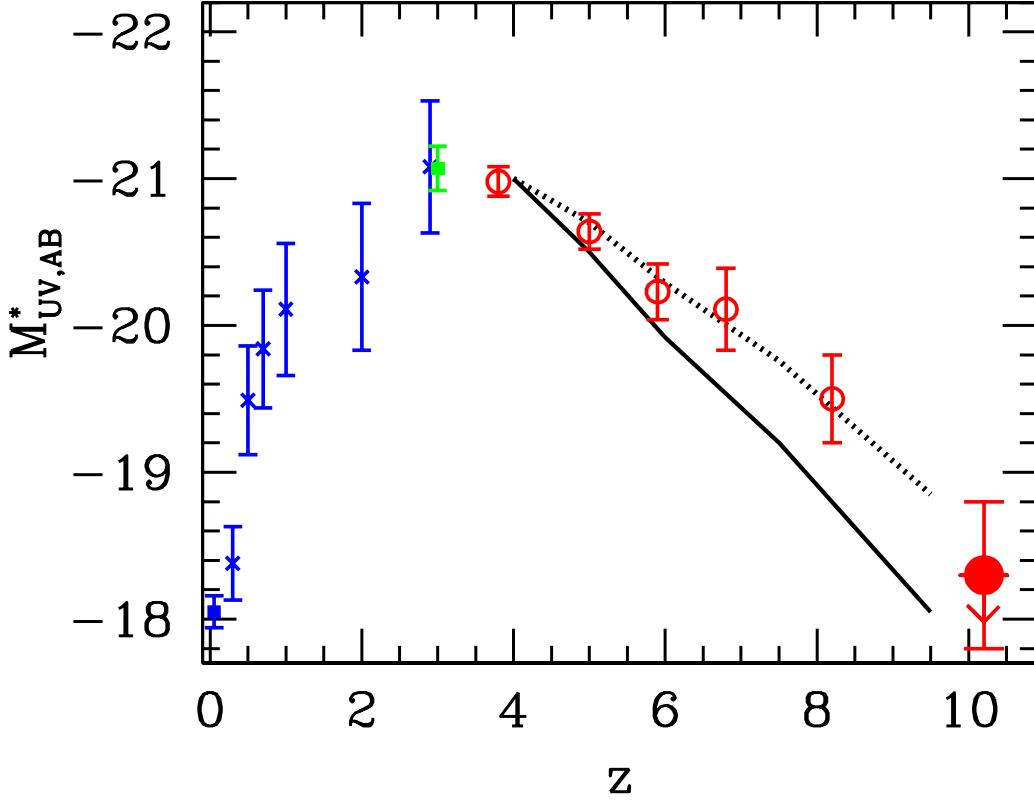


Fig. 9.— J_{125} -dropout search results expressed as constraints on the characteristic luminosity $M_{UV,AB}^*$ at $z \sim 10$. ϕ^* is taken to be 0.0012 Mpc^{-3} for the $z \sim 10$ fit (similar to the values found at $z \sim 3$ -8^{1,22}) while α is fixed to -1.74 – the same value as found at $z \sim 6$.¹ The $z \sim 10$ constraint is shown as a solid circle based upon an estimate of 0.8 probable J_{125} -dropout candidates and as an upper limit (assuming none of our candidates correspond to $z \sim 10$ galaxies). These are essentially identical given our single $z \sim 10$ candidate. Also shown are the characteristic luminosities estimated for the UV LF at $z \lesssim 8$.^{1,2,3,22,50} The solid black line shows the evolution predicted from the halo mass function⁵¹ assuming a mass-to-light ratio which is constant while the dashed black line shows this evolution assuming a mass-to-light ratio which varies as $(1+z)^{-1}$. These lines are identical to those in Figure 10 of Bouwens et al.²². While it is unclear whether the UV LF at $z \sim 10$ is well represented by a Schechter function and whether ϕ^* and α remain relatively constant over this redshift interval, the characteristic luminosity M^* seems to be a convenient one-parameter way of characterizing the evolution of the UV LF over a wide redshift range. From this figure, it is clear that observed evolution in the UV LF reported from $z \sim 8$ to $z \sim 4$ continues out to $z \sim 10$.

are used to estimate the effective search volume as a function of absolute magnitude. Both the wide-area ERS and ultra-deep HUDF searches are included in these effective volume estimates. These volumes implicitly include the effects of incompleteness and are an integral of the selection efficiencies with redshift (Figure S8). The LF is then equal to the number of $z \sim 10$ candidates found divided by these effective volumes. Based upon our contamination estimates (§7), we assume that 0.8 J_{125} -dropout candidates in our HUDF09 selection are probable $z \sim 10$ galaxies, but also consider the possibility that none correspond to $z \sim 10$ galaxies. Our stepwise LFs are presented in Figure 3 of the main text.

It is also interesting to examine the present LF results in terms of a Schechter parametrization, given the utility such parametrizations have had in modelling the LF over a wide range in redshifts (though we recognize that this parameterization may not be appropriate at $z \sim 10$). Again we consider two cases, first that 0.8 J_{125} -dropout candidates from our HUDF09 selection correspond to $z \sim 10$ galaxies and second that no candidates do. To quantify the constraints we can set on the Schechter parameters at $z \sim 10$, we calculate the number of J_{125} -dropouts we would expect to find to these magnitude limits, using the selection efficiencies we can infer from the simulation results in §9. For simplicity, we consider the constraints on the characteristic luminosity M^* at $z \sim 10$, if the normalization ϕ^* and faint-end slope α is equal to $\sim 0.0012 \text{ Mpc}^{-3}$ and ~ -1.74 – similar to that found at lower redshift $z \sim 4 - 6$.^{1,22} In detail, we find that $M_{UV}^* = -18.3 \pm 0.5$ AB mag at $z \sim 10$, assuming that 0.8 J_{125} -dropout candidates from the present sample are at $z \sim 10$. In the case that none are, $M_{UV}^* > -18.3$ AB mag at $z \sim 10$, which is $\gtrsim 2.5$ mag fainter than the $M_{UV,AB}^* \sim -21$ AB mag derived^{1,28} at $z \sim 4$ and the $M_{UV,AB}^* \sim -19.5 \pm 0.3$ estimated³ at $z \sim 8$ – illustrating how dramatically the UV LF is evolving at high redshift. While we have no evidence that the UV LF maintains a Schechter parametrization out to $z \sim 10$ with a relatively constant ϕ^* and α , parametrizing the evolution in terms of the characteristic luminosity M^* does provide us with a convenient way of quantifying the overall rate of evolution in the UV LF.

11. Constraints on the UV Luminosity Density/SFR density at $z \sim 10$

The present J_{125} -dropout searches permit us to set constraints on the luminosity density at $z \sim 10$ brightward of $0.06 L_{z=3}^*$. To derive these constraints, we integrate up the LF results from §10 to the survey limits. Again, we consider the case that 0.8 J_{125} -dropout candidates from our selection correspond to $z \sim 10$ galaxies and the case that none do. The derived UV luminosity densities are then converted into the equivalent SFR densities, adopting the Madau et al.⁵² conversion factor. The Madau et al.⁵² conversion factor assumes a constant rate of star formation for $\gtrsim 100$ Myr. This suggests that it may be inappropriate to use this conversion at $z \sim 10$. Interestingly, the time scale inferred for star-formation in star-forming galaxies at $z \sim 7-8$ is nonetheless quite extended,^{12,13} with inferred ages of $\sim 300-400$ Myr. This suggests that even at $z \sim 10$ it may not be unreasonable to suppose that galaxies experience extended star-formation for $\gtrsim 100$ Myr. However, we recognize that the Madau et al.⁵² approach, while convenient, is limited, and look forward to more sophisticated

analyses in the future.⁵³

The results are presented in Table S2 and Figure 4 of the main text, alongside our most recent results at $z \sim 7$ and $z \sim 8$.⁹ Since essentially all galaxies in the luminosity range of our samples (i.e., $\gtrsim -19.5$ AB mag) show very blue UV -continuum slopes β ($\beta \lesssim -2.5$) at $z \gtrsim 5$,^{25,49} no dust obscuration is assumed in the SFR density estimates at high redshift.

Table 2. *UV* Luminosity Densities and Star Formation Rate Densities.^a

Dropout Sample	$\langle z \rangle$	$\log_{10} \mathcal{L}$	\log_{10} SFR density	
		(ergs s^{-1} $\text{Hz}^{-1} \text{Mpc}^{-3}$)	($M_{\odot} \text{Mpc}^{-3} \text{yr}^{-1}$) Uncorrected	Corrected ^b
z^9	6.8	25.80 ± 0.10	-2.10 ± 0.10	-2.10 ± 0.10
Y^9	8.0	25.57 ± 0.11	-2.33 ± 0.11	-2.33 ± 0.11
J (This work: 0.8 candidates)	10.3	$24.29^{+0.51}_{-0.76}$	$-3.61^{+0.51}_{-0.76}$	$-3.61^{+0.51}_{-0.76}$
J (This work: no candidates)	10.3	$< 24.42^c$	$< -3.48^c$	$< -3.48^c$

^aIntegrated down to ~ -17.9 AB mag.

^bThe blue *UV*-continuum slopes $\beta \lesssim -2.5$ observed at $z \sim 7-8$ suggest very little dust extinction.^{2,3,49} As a result, the corrected and uncorrected SFR densities are the same.

^cUpper limits here are 1σ (68% confidence).

12. References

31. Magee, D. K., Bouwens, R. J., & Illingworth, G. D. NICRED: A NICMOS Image Processing Pipeline, *Astronomical Data Analysis Software and Systems XVI*, **376**, 261 (2007).
32. Koekemoer, A. M., Fruchter, A. S., Hook, R. N., & Hack, W. MultiDrizzle: An Integrated Pyraf Script for Registering, Cleaning and Combining Images, *The 2002 HST Calibration Workshop : Hubble after the Installation of the ACS and the NICMOS Cooling System*, 337 (2002).
33. Giavalisco, M., et al. The Great Observatories Origins Deep Survey: Initial Results from Optical and Near-Infrared Imaging, *Astrophys. J. Lett.*, **600**, 93-98 (2004).
34. Riess, A. G., et al. New Hubble Space Telescope Discoveries of Type Ia Supernovae at $z \geq 1$: Narrowing Constraints on the Early Behavior of Dark Energy, *Astrophys. J.*, **659**, 98-121 (2007).
35. Bouwens, R.J., Illingworth, G.D., Blakeslee, J.P., & Franx, M. Galaxies at $z \sim 6$: The UV Luminosity Function and Luminosity Density from 506 UDF, UDF-Ps, and GOODS i-dropouts, *Astrophys. J.*, **653**, 53-85 (2006).
36. Bouwens, R.J., Broadhurst, T.J., Illingworth, G.D. Cloning Dropouts: Implications for Galaxy Evolution at High Redshift, *Astrophys. J.* **593**, 640-660 (2003).
37. Bertin, E. & Arnouts, S. SExtractor: Software for source extraction, *Astron. Astrophys. Suppl.*, **117**, 393-404 (1996).
38. Kron, R. G. Photometry of a complete sample of faint galaxies, *Astrophys. J. Suppl.*, **43**, 305-325 (1980).
39. Szalay, A. S., Connolly, A. J., & Szokoly, G. P. Simultaneous Multicolor Detection of Faint Galaxies in the Hubble Deep Field, *Astron. J.*, **117**, 68-74 (1999).
40. Labbé, I., Bouwens, R., Illingworth, G. D., & Franx, M. Spitzer IRAC Confirmation of z_{850} -Dropout Galaxies in the Hubble Ultra Deep Field: Stellar Masses and Ages at $z \sim 7$, *Astrophys. J. Lett.*, **649**, 67-70 (2006).
41. Coleman, G. D., Wu, C.-C., & Weedman, D. W. Colors and magnitudes predicted for high redshift galaxies, *Astrophys. J. Suppl.*, **43**, 393-416 (1980).
42. Knapp, G. R., et al. Near-Infrared Photometry and Spectroscopy of L and T Dwarfs: The Effects of Temperature, Clouds, and Gravity, *Astron. J.*, **127**, 3553-3578 (2004).
43. Oesch, P. A., et al. The UDF05 Follow-Up of the Hubble Ultra Deep Field. II. Constraints on Reionization from Z-Dropout Galaxies, *Astrophys. J.*, **690**, 1350-1357 (2009).
44. Whitelock, P., et al. Mass-losing stars in the South Galactic CAP, *Month. Not. R. Astron. Soc.*, **276**, 219-254 (1995).

45. Dickinson, M., et al. The Unusual Infrared Object HDF-N J123656.3+621322, *Astrophys. J.*, **531**, 624-634 (2000).
46. Bouwens, R. J., Illingworth, G. D., Blakeslee, J. P., Broadhurst, T. J., & Franx, M. Galaxy Size Evolution at High Redshift and Surface Brightness Selection Effects: Constraints from the Hubble Ultra Deep Field, *Astrophys. J. Lett.*, **611**, 1-4 (2004).
47. Ferguson, H. C. et al. The Size Evolution of High-Redshift Galaxies, *Astrophys. J. Lett.*, **600**, 107-110 (2004).
48. Oesch, P.A., et al. Structure and Morphologies of $z \sim 7-8$ Galaxies from Ultra-deep WFC3/IR Imaging of the Hubble Ultra-deep Field, *Astrophys. J.*, **709**, 21-25 (2010).
49. Bouwens, R. J., et al. Very Blue UV-Continuum Slope β of Low Luminosity $z \sim 7$ Galaxies from WFC3/IR: Evidence for Extremely Low Metallicities?, *Astrophys. J. Lett.*, **708**, 69-73 (2010).
50. Arnouts, S., et al. The GALEX VIMOS-VLT Deep Survey Measurement of the Evolution of the 1500Å Luminosity Function, *Astrophys. J. Lett.*, **619**, 43-46 (2005).
51. Sheth, R. K. & Tormen, G. Large-scale bias and the peak background split, *Month. Not. R. Astron. Soc.*, **308**, 119-126 (1999).
52. Madau, P., Pozzetti, L. & Dickinson, M. The Star Formation History of Field Galaxies, *Astrophys. J.*, **498**, 106-116 (1998).
53. Verma, A., Lehnert, M. D., Förster Schreiber, N. M., Bremer, M. N., & Douglas, L. Young Galaxies in the Early Universe: The Physical Properties of Luminous $z \sim 5$ LBGs Derived from Their Rest-frame UV to Visible SEDs, *Month. Not. R. Astron. Soc.*, **377**, 1024-1042 (2007).

A. Assessment of our First-year J_{125} Dropout Selection

Shortly after the first-year of ultra-deep WFC3/IR observations over the HUDF were obtained, we carried out a search for $z \sim 10$ J_{125} -dropout candidates. Three J_{125} -dropout candidates were identified. These candidates showed 5σ detections in scalable elliptical apertures and had measured $J_{125} - H_{160}$ colors > 1.2 . They showed no significant detection in the optical data. These three J_{125} -dropout candidates also showed no significant detection in the IRAC 3.6μ and 4.5μ observations – consistent with the much shallower depths of the IRAC observations. These candidates plausibly corresponded to star-forming galaxies at $z \sim 10$. See Bouwens et al. arXiv:0912.4263 for details.

The availability of a second year of ultra-deep WFC3/IR observations over the HUDF (25 orbits in the H_{160} band) provided us with the opportunity to test the robustness of these candidates. If real, one would have expected the candidates to be detected at $\geq 3.5\sigma$ in the new observations.

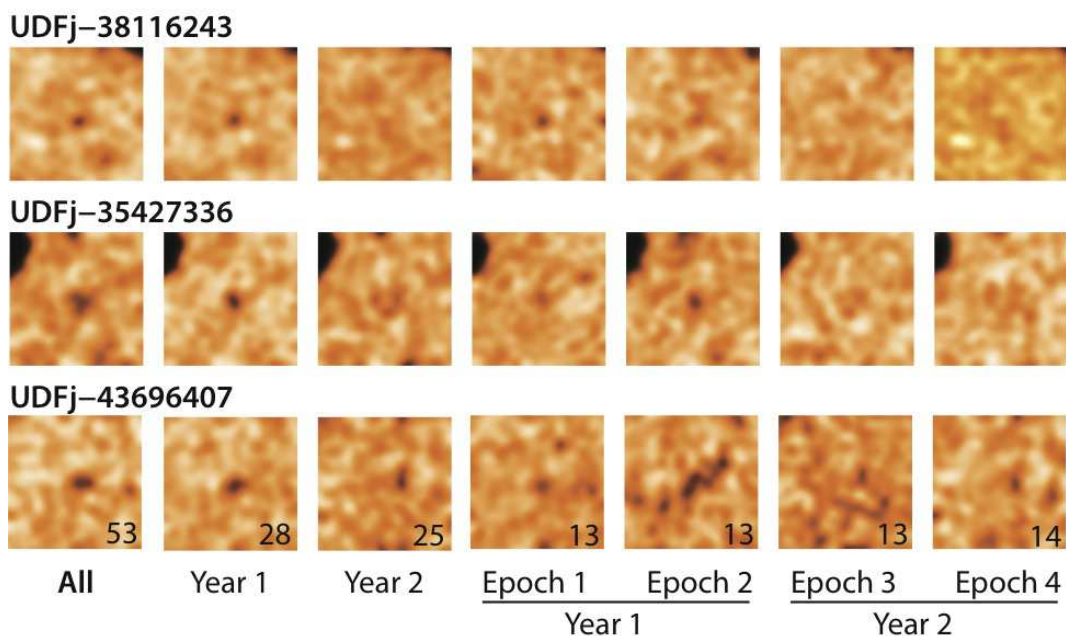


Fig. 10.— Appearance of the $z \sim 10$ J_{125} -dropout candidates we had identified in the first-year data in different subsets of the full data set. Shown is their appearance in the full data set, in the first and second year data, and in 13-orbit subsets of the ultra-deep WFC3/IR H_{160} -band observations over the HUDF (53 orbits in total). The number of orbits of observations for each subset is given in the lower right corner. While these candidates are visible at modest significance in the two 50% splits of the first-year data, they are not visible at much significance in the two 50% splits of the second-year data (and hence cannot be considered to be robust candidates in the full data set: see Appendix A).

Figure S10 shows the new observations we have for our three candidates, the first-year observations and the full two-year observations considered together. Strikingly, two of the candidates are not even significant at 1σ in the new observations, which suggests two candidates from the first-year observations were simply spurious. For the third candidate UDFj-38116243, a 1.3σ detection is found at the position of the source. While this is consistent with the candidate UDFj-38116243 corresponding to an actual source (with an apparent magnitude at least 1 mag fainter than what we estimated from the first-year observations), we no longer consider UDFj-38116243 to be a viable $z \sim 10$ candidate. The large discrepancy between the 5.6σ detection in the first year observations and the 1.3σ detection in the second year observations gives us little confidence that UDFj-38116243 is a real source and suggests that it may be spurious.

This is surprising, given the nominal detection of the three candidates in the first year observations at $\sim 5\sigma$, the visibility of the candidates in 50% subsets of that first-year data, and the apparent detection of two of the candidates in the NICMOS H_{160} -band data. Nonetheless, the fact that all three candidates were identified close to the 5σ completeness limit of the first-year observations – where the contamination increases relatively rapidly as the S/N decreases further – indicated that the candidates were not the most robust (as we noted).

How is it possible that apparent 5σ detections might not prove to be robust? A primary reason is the way in which the apertures were defined. In searching for possible 5σ detections in the first-year observations, we utilized scalable Kron-style apertures (Kron [1980] factor of 1.2). Such apertures – while working very well to measure the fluxes for faint sources – can lead to biased measurements of source significance. This is because the apertures that are used to evaluate the significance of the sources are also established by the same apparent flux distribution. This can lead to overestimates of the significance by as much as 0.5σ to 1.0σ for $\sim 4\sigma$ sources, and so some sources that are really $< 5\sigma$ can appear at $> 5\sigma$. Even for purely Gaussian noise, one would expect a modest number $\gtrsim 3$ of purely spurious $\sim 4\sigma$ candidates.

A second contributing factor is our slight underestimate of the noise in the first-year observations. The extent of the underestimate appears to have been just 5%, as obtained from our current estimates of the noise where we actually fit to the full noise distribution (i.e., Figure S5), but this is large enough to make a 4.7σ fluctuation look like a 5σ fluctuation.

Third, as expected, there appears to have been a very slight non-Gaussianity to the noise distribution. While it is remarkably Gaussian to large σ (Figure S5), the small non-Gaussianity present could possibly have enhanced the number of spurious sources with apparent ~ 4 - 5σ significance levels over that expected from Gaussian statistics by 50%. The factor is quite poorly determined, however, since it is quite challenging to establish deviations from Gaussianity at $\sim 4\sigma$. The existence of a $\sim 5\sigma$ single-band detection in the 34-orbit J_{125} -band image (see §7) provides some evidence that non-Gaussianity could play a role, but we emphasize that such effects are likely to be less important in the full two-year 53-orbit H_{160} -band data (which consisting of a larger number of exposures should have more Gaussian noise properties).

Fourth, we now realize that the tests we used for establishing the level of contamination from spurious sources led to an underestimate of the prevalence of those sources. This is likely to be a significant issue with our earlier analysis. We have realized that our previous simulations likely suffered from two shortcomings which caused us to underestimate the number of spurious sources significantly. We did not include (1) the expected population of very faint (“below-the-limit”) $\sim 30\text{--}33$ mag sources in the simulations and (2) large foreground sources. The expected population of faint sources (1) would act to significantly increase the number of positive σ fluctuations. By ignoring this effect, we significantly underpredicted the number of spurious sources. (2) The effect of bright sources may not be as significant, but they would also play a role by making the sky background more difficult to determine (some empty regions of the image are on the wings of bright objects and some regions are not). This would result in significant underestimates of the sky levels for many sources and hence overestimates of their significance levels. By not including bright sources, our simulations would not account for the effect they would have on the background estimates, and hence we could easily have underpredicted the number of spurious sources present in the real observations.

Taken together these results show that no one factor was dominant in why the sources proved to be unreliable. Probably the most significant factor was that the flux in the candidates was overestimated by the use of the scalable elliptical apertures (by 5-15%). This, combined with the slight underestimate of the noise level in the data (by 5%), meant that the S/N of the sources was not $>5\sigma$, but $<5\sigma$, and closer to 4σ . Since the likelihood of contamination from spurious sources increases exponentially as the S/N decreases, the contamination rate was not the small numbers expected for $S/N > 5$, but the much larger rate for $S/N \sim 4$. The spurious source contamination rate was likely an order of magnitude (or more) larger.

In summary, the combination of (1) the sources being fainter than we derived from the scalable aperture and (2) the noise being underestimated led to our selecting sources that had lower S/N than 5σ . For such sources the spurious source contamination rate was much higher. These factors combined to make it much more likely that the sources were spurious (in two cases) or, at best, much less significant (the other case of the three). The unfortunate coincidence of a marginal signal (and likely spurious event also) in the NICMOS observations gave us an added sense of security that proved unwarranted.